Faculdade de Engenharia da Universidade do Porto

Estimation of choroidal thickness in OCT images

Simão Pedro Marques Pinto de Faria

Master in Bioengineering
Major in Biomedical Engineering

Supervisor: Prof. Dr. Ana Maria Mendonça
Co-supervisor: Prof. Dr. Jorge Alves da Silva

July of 2016

Abstract

It is proven that the choroidal thickness is a sign for multiple eye diseases. The changes in the layer's thickness can be caused by an infection in the eye globe, dehydration, high myopia, old age and others. Optical Coherence Tomography (OCT) is a recent imaging technique that allows the visualization of tomographic images of near surface tissues like those in the eye globe. Deeper tissues, like the choroid, are more affected by noise and shadows cast by the above structures, hampering their visualization. When the Enhanced Depth Imaging (EDI) OCT was developed, the automatic measurement of the thickness of the choroid became more viable. This technique allows a better definition of the choroidal limits, essential for the correct calculation of the tissue's thickness. Some of the main advantages of the automatic calculation of the choroidal thickness are the speed of large scale measurements, the subjectivity reduction of manual image analysis and a possible improvement of data visualization, allowing the ophthalmologist a better experience in the analysis of the OCT.

In order to execute the automatic estimation of choroidal thickness, this work was separated in three main steps: the preprocessing, the delineation of the inner and outer choroidal boundaries (ICB and OCB) and the calculation of the choroidal thickness. The preprocessing includes contrast adjustment for each boundary, reduction of shadows cast by retinal vessels and speckle noise reduction made with Stationary Wavelet Transform (SWT). The delineation of both ICB and OCB is achieved with a minimum path algorithm. The difference in calculation of the two boundaries is in the weight matrices that define the cost of the connections between nodes. The weight matrices are calculated with different image filtering techniques according to the boundary's characteristics. The choroidal thickness calculation is simply the average distance between the two segmented limits. After the calculation of the choroidal thickness, an additional step is made to interpolate and align the results of two sets of OCT images of the same eye, scanned in perpendicular directions. Interpolation and alignment of results allow a comparison between the segmentations made in both directions.

Final results were compared with two sets of manual markings of the OCB. The mean absolute errors of automatic delineation were, in most cases, lower than the errors between two manual markings, evidencing a good outcome for the automatic method, taking as a reference the manual measurements, with their natural variation. The comparison between the choroidal thickness calculated in the two directions was very satisfying in the majority of the choroidal area, having a median of the difference of approximately 2.2% of the average choroidal thickness. The maximum difference obtained was about 52% of the average choroidal thickness, however the major differences in the segmentation were in areas usually hard to segment. These results show that the algorithm properly calculates the choroidal thickness. However, more OCT images should be tested to prove the robustness of this algorithm.

Resumo

Está provado que a espessura da coroide é um sinal de múltiplas doenças. A alteração da espessura desta camada pode ser causada por uma infeção no globo ocular, desidratação, miopia de alto grau, idade avançada, entre outros. A Tomografia de Coerência Ótica (OCT) é uma recente técnica imagiológica que permite a visualização de imagens tomográficas de tecidos superficiais, como os do globo ocular. Tecidos mais profundos, como a coroide, são mais afetados pelo ruído e por sombras projetadas pelos tecidos acima, dificultando a sua visualização. Quando a técnica de *Enhanced Depth Imaging* (EDI) OCT foi desenvolvida, a medição automática da espessura da coroide tornou-se mais viável. Esta técnica permite uma melhor definição dos limites da coroide, essenciais para o cálculo correto da sua espessura. Algumas das vantagens principais do cálculo automático da espessura da coroide são a rapidez de medições em larga escala, a redução da subjetividade da análise manual das imagens e a capacidade de melhorar a visualização dos dados, permitindo ao oftalmologista uma melhor experiência na análise do OCT.

Para estimar automaticamente a espessura da coroide, este trabalho foi dividido em três partes: uma de pré-processamento, outra de delineação os limites interior e exterior da coroide (ICB e OCB) e finalmente o cálculo da espessura da coroide. A fase de pré-processamento inclui o ajuste do contraste para cada limite, a redução das sombras dos vasos da retina e a redução do ruído *speckle* da imagem, feito com recurso à Transformada Estacionária com Ôndula (SWT). O delineamento dos ICB e OCB é feito com um algoritmo de caminho mínimo. A diferença no cálculo dos dois limites vêm das diferentes matrizes de pesos que definem os custos das conexões entre nós. Estas matrizes de custos são calculadas com recurso a diferentes técnicas de filtragem de imagens, de acordo com as características do limite interior ou exterior. O cálculo da espessura da coroide é executado através da média da distância entre os dois limites. Após o cálculo da espessura, é feito um passo adicional para interpolar e alinhar os resultados de dois conjuntos de imagens de OCT adquiridas em direções perpendiculares. A interpolação e alinhamento dos resultados permitem uma comparação entre as segmentações feitas nas duas direções.

Os resultados finais foram comparados com dois conjuntos de marcações manuais do OCB. Os erros absolutos médios da delineação automática foram, na maioria dos casos, mais baixos do que os erros entre as duas marcações manuais, evidenciando os bons resultados do método automático tomando como referência as marcações manuais, com os seus desvios naturais. A comparação entre a espessura da coroide calculada nas duas direções foi bastante satisfatória para a maior parte da área coroideia, sendo a mediana da diferença apenas de aproximadamente 2,2% da espessura média da coroide. A diferença máxima obtida foi cerca de 52% da espessura média, no entanto, essa diferença foi obtida em áreas difíceis de segmentar

a coroide. Os resultados mostram que o algoritmo calcula de forma adequada a espessura da coroide. No entanto, deveriam ser feitos testes com mais imagens para confirmar a robustez deste algoritmo.

Acknowledgments

The author would like to thank:

Dr. Susana Penas, from Serviço de Oftalmologia of Hospital de S. João do Porto, for providing the images, manual markings and medical advice for the development of this work.

Dr. Luís Mendonça, from Serviço de Oftalmologia of Hospital de Braga, for providing additional markings used in this work.

The supervisors, Prof.ª Dr.ª Ana Maria Mendonça and Prof. Dr. Jorge Alves da Silva from the Department of Electrical and Computer Engineering and the Department of Informatics Engineering, for the assistance given in all the development of the work.

INESC-TEC for the provided means, tools and support for the execution of this work.

FCT and INESC-TEC for granting a PEst scholarship during the development of this work.

Index

Figure List

Table List

Abbreviations

BM	Bruch's Membrane
CSI	Choroidal Scleral Interface
EDI	Enhanced Depth Imaging
GUI	Graphical User Interface
ICB	Inner Choroidal Boundary
IZ	Interdigitation Zone
IR	Infrared Reflectance
OCB	Outer Choroidal Boundary
OCT	Optical Coherence Tomography
RPE	Retinal Pigment Epithelium
SWT	Stationary Wavelet Transform
3D	Three Dimensional

Chapter 1

Introduction

Vision is the window that allows the experience of the world. As one of the most important human senses, it gathers the light information in a range of wavelengths to enable a better interaction with the surrounding reality. Visual cues can help the human-being, for instance, with the detection of visible objects, self-balance, recognizing faces, understanding written words and interacting with the world around them. Because it is such a fundamental key of the way we sense our lives, sometimes people tend to take it for granted, only reminding ourselves the impact of the eye when the light is scarce and we fail to follow a simple path without major deviations or startling stumbles.

The development of optical and medical technologies allowed ophthalmology to reach greater and greater achievements in the knowledge of the eyesight and to discover simpler methods of treatment. One relevant example of a new technology from which ophthalmology benefited is the Optical Coherence Tomography (OCT). Developed in 1990[1], the technique uses interferometry properties of low coherence light to observe the various layers of the scattering media, in this case, the ocular globe.

Advantages of the OCT for ophthalmology are: it is a cheap, harmless, practical technology that allows the monitoring of the deep layers of the eye in vivo and with a good resolution, giving doctors the ability to observe changes in those structures that might impair patients' vision, like infections and tissue lesions.

Choroidal thickness can be an indicator of the health of the retina and ultimately a sign of a probable impairment in the eyesight. It started to be used as a medical sign with the increase of the OCT popularity, as it can change with the presence of a pathology or other factors. The choroid normally thickens with some pathologies such as *retinitis pigmentosa*[2], serous chorioretinopathy[1], diabetic retinopathy[3] and others that cause inflammation in the tissue. However, the choroid might also narrow, which normally happens in patients with a higher refractive error (myopia)[4] and with aging[5].

Analysis of OCT B-scans (tomographic images of an OCT) is always necessary and conclusions should not be taken exclusively on the measurement of the choroidal thickness, but the automatic calculation of this measure should help the clinician to achieve better diagnosis.

Although the OCT can be very useful for the health professionals, it can generate great amounts of data to be analyzed. If doctors want to measure the thickness of the choroid, they have to analyze multiple segments in each cross section of the OCT B-scan, and still, data can be misinterpreted. The development of an automatic method for the segmentation of the choroid should allow a better use of the potentialities of the OCT, with less monotonous manual thickness measurements. An automatic methodology should also eliminate some of the variability in the delineation of the choroid, as the manual markings often variate according to the observer, especially when an incoming vessel is interpreted as part of the choroid by one individual and not by another.

1.1 - Motivation

Due to the fact that OCT loses power with tissue penetration and the choroid layer is located behind the retina, its visualization is always worse than more superficial tissues. Recent improvements in the image quality and acquisition made this layer a lot more distinct, like in the Enhanced Depth Imaging (EDI) OCT. These technological advancements also raised a new opportunity to automatically segment the choroid.

The thickness of the choroid started to be used as a medical sign for different pathologies with the increase of popularity of the OCT. The automatic calculation of the choroidal thickness should help clinicians to achieve a better diagnosis.

The innovation of the OCT and the relevance of this automatic solution were the main motivations for the development of this work, as well as the opportunity to obtain experience in medical image processing areas allied with the challenge of working with a different type of imaging technique.

1.2 - Aims

The goal of this project is to develop a software system with the ability to accurately segment the choroidal layer and measure its thickness.

The full automation of the methodology, from the selection of useful information from the provided OCT B-scans videos, to the display of the final results, is one of the objectives. The proposed approach contains three main phases: an initial stage of preprocessing where the given data is selected and filtered to prepare the image for further processing; a second stage for the delineation of the two interfaces that limit the choroid: the Bruch's Membrane (BM) and Choroidal-Scleral Interface (CSI); and finally, the measurement of the choroidal thickness and the possible comparison of results of overlapping scans.

An intuitive user interface for the interaction with the system is also an aim, because it is important to improve the usability of all its capabilities.

1.3 - Overview of the dissertation

This dissertation describes the work that was developed for the estimation of the choroidal thickness in OCT images. After the thickness calculation, two B-scan sets of the same eye can be combined to compare the limits obtained from different images of the same eye.

The next chapter is devoted to the clarification of some prevalent topics necessary in the developed work. The technique of the OCT will be more thoroughly addressed, as well as some important aspects about the choroid and some image processing algorithms used in this project.

The third chapter contains the description of the developed software system and clarification of its main steps.

The fourth chapter will focus on the developed work for the combination of information from two different B-scan sets of the same eye. Differences in the direction of the acquisition, may generate changes in the delineation of the choroidal boundaries, solely because of the blood vessels' sections scanned. Misalignments in the scanned region are corrected for the comparison between the measures in both sets.

The fifth chapter includes a description of the graphics user interface (GUI), created for the execution of the choroidal thickness measurement algorithm.

Results and their analysis are presented in the sixth chapter. There, the obtained measures and segmentations are compared to some manually delineated CSIs and the consistency of the results is analyzed. Consequent comments evaluate the algorithm's performance and add some ideas on what could be improved.

In the final chapter, the concluding notes are presented, and a critical analysis to the accomplished work is made.

Chapter 2

State of the Art

2.1 - Choroid

The choroid is the portion of the vascular tunic located in the eye globe. It can be found between the retinal and scleral layers as shown in Figure 2.1. The retina is the interior layer which contains the sensory cells of the eye and is separated from the choroid by the BM or inner choroidal boundary (ICB) while the sclera is a more uniform layer on the exterior of the eyeball and has a more structural function. The inner limit of the sclera is the CSI or outer choroidal boundary (OCB).

By contrast, the choroid is the most vascular layer of the three with the main objective of enabling the diffusion of nutrients and oxygen to the retina and regulate ocular pressure and temperature[6]. Even though the light sensitive cells have high metabolic rates, the retina has a low quantity of vessels that block light and may hamper vision, so the metabolic necessities are granted by the choroid being even essential for the macula region and optic nerve.

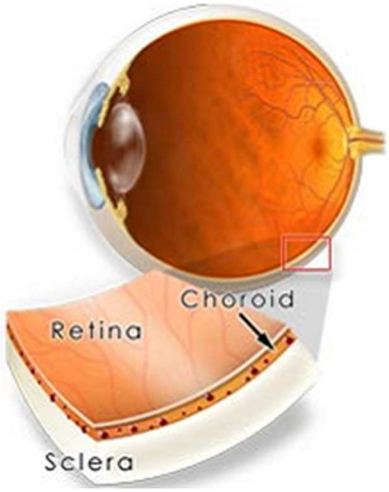

Figure 2.1 – Anatomical model of the eye with a detailed view of the eye globe tissues (retina, choroid and sclera). Image source: St. Luke's Cataract and Laser Institute.

The OCT is the most appropriate medical imaging technique to visualize the choroid. The OCT has good enough resolution to observe the choroid's thin details and, with the technological processing advances, its depth range is sufficient to reach the choroid (that has a mean thickness of (272±81μm)[5]). In Figure 2.2, different structures visible in an OCT B-scan are captioned, according to the International Nomenclature for Optical Coherence Tomography Panel[7]. The nomenclature used in this thesis includes the following terms: Bruch's layer or Bruch's Membrane BM (many times indistinguishable from the RPE – Retinal Pigmented Epithelium), Choroid Sclera Junction or Choroidal-Scleral Interface (CSI) and Interdigitation Zone (IZ).

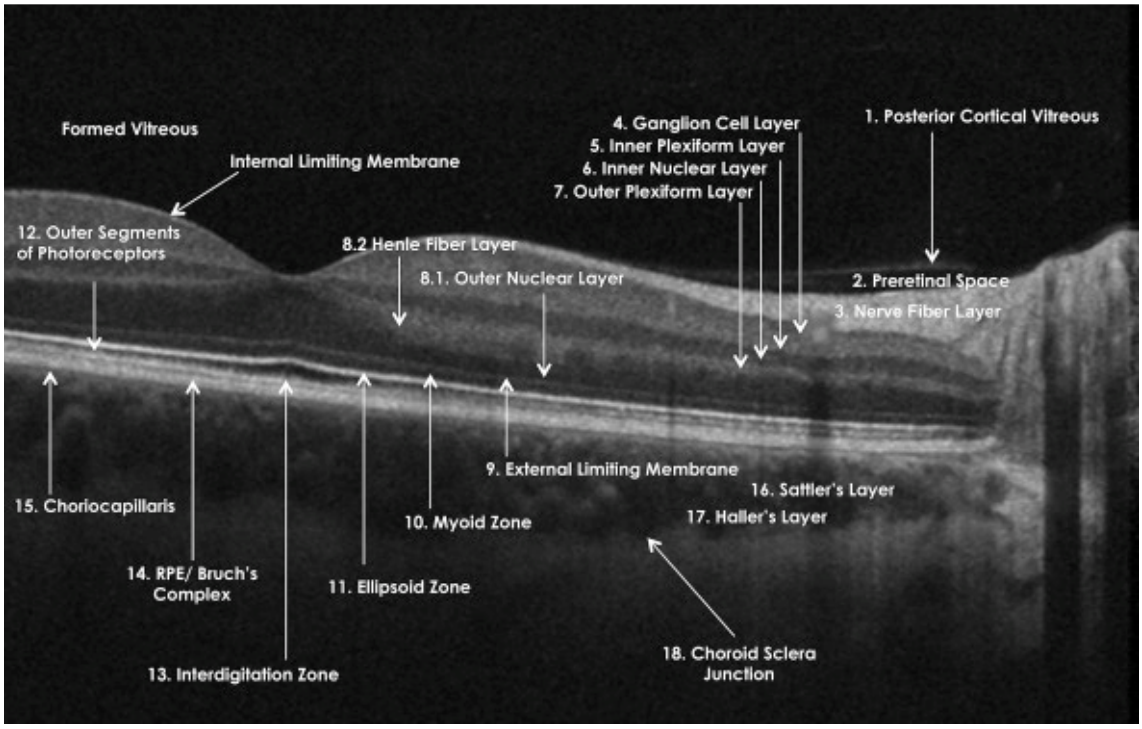

Figure 2.2 – OCT image of the eye globe where each observable zone is captioned, according to the International Nomenclature for OCT Panel. Image source: [7].

2.2 - Optical Coherence Tomography

OCT, as the name suggests, uses the light coherence property to obtain a series of cross-sections, in this case used to observe the eye globe layers. Some advantages of this technique are the ability to visualize some deep tissues in vivo, the practicality (no need for contrast or other preparation), the safety for the patient and the overall cost.

In the graph presented in Figure 2.3, different tomography imaging methods are compared, by resolution and depth of penetration. Compared to other in vivo methods, OCT is the only technique capable of analyzing tissues such as the choroid. The OCT has enough depth range to reach the choroid and a good resolution to observe the layer's characteristics.

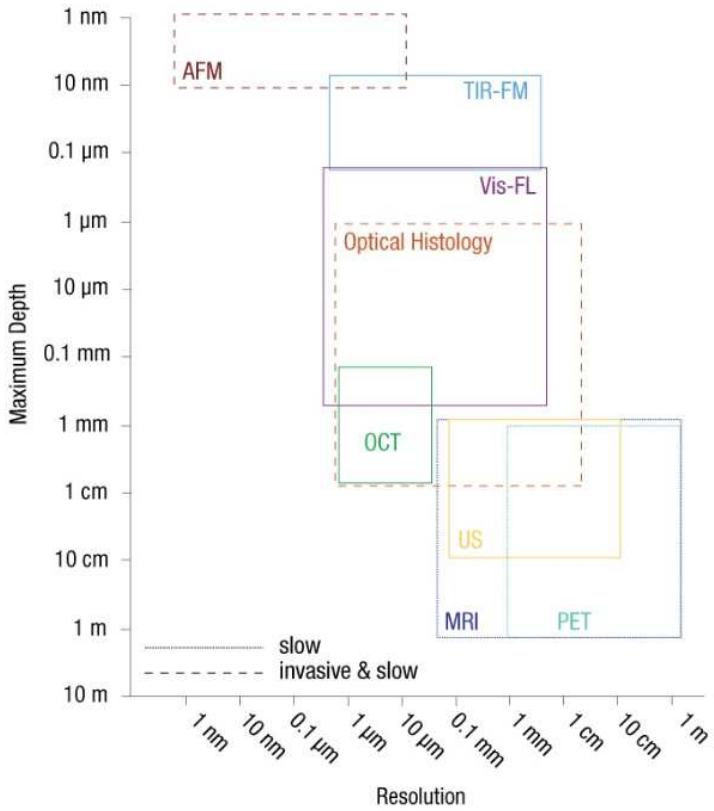

Figure 2.3 – Comparison between different tomography imaging techniques by resolution and maximum depth. AFM - Atomic Force Microscopy; TIR-FM – Total Internal Reflection Fluorescence Microscopy; Vis-FL – Visual Florescence Light microscopy; OCT - Optical Coherence Tomography; US – Ultrasound; MRI – Magnetic Resonance Imaging; PET – Positron Emission Tomography. Image source: [8].

The OCT image starts by the detection of an A-scan (one dimensional vector that corresponds to the data along the depth of the scattering media). In a simple OCT A-scan, a beam of low coherent light is split in two; one is directed to the sample to analyze where it scatters, while the other heads for a moving reflective mirror to serve as a reference. The two divided beams meet again and the power of the combined beam is calculated[9]; this power depends on the intensity of the scattered beam when the two beams are coherent - both distances travelled by the beams are similar. To obtain an A-scan, the moving reference mirror has to travel in order to measure the power of the sample beam in throughout the depth of the eye wall. Similarities in phase of the two beams enable the calculation of the distances of the layers where the light scattered back.

To avoid the movement of the reference mirror, a frequency domain OCT was developed, where the distances in the scattering media can be calculated using the Fourier transform information of the signal that results from the interference of the two beams[10]. The different resulting frequencies can be optically separated and detected in an array sensor; this data is then converted into the whole A-scan. Because the A-scan is obtained in one iteration, the scanning of the desired surface can be approximately six times faster with half the resolution.

Figure 2.4 represents the acquisition of an OCT A-scan in both Time Domain and Frequency Domain OCT where the main differences, like the moving or fixed reference mirror and the use of the Fourier transform, can be seen. In both techniques the B-scan is obtained by joining multiple A-scans scanned along the same plane, transforming them in an image.

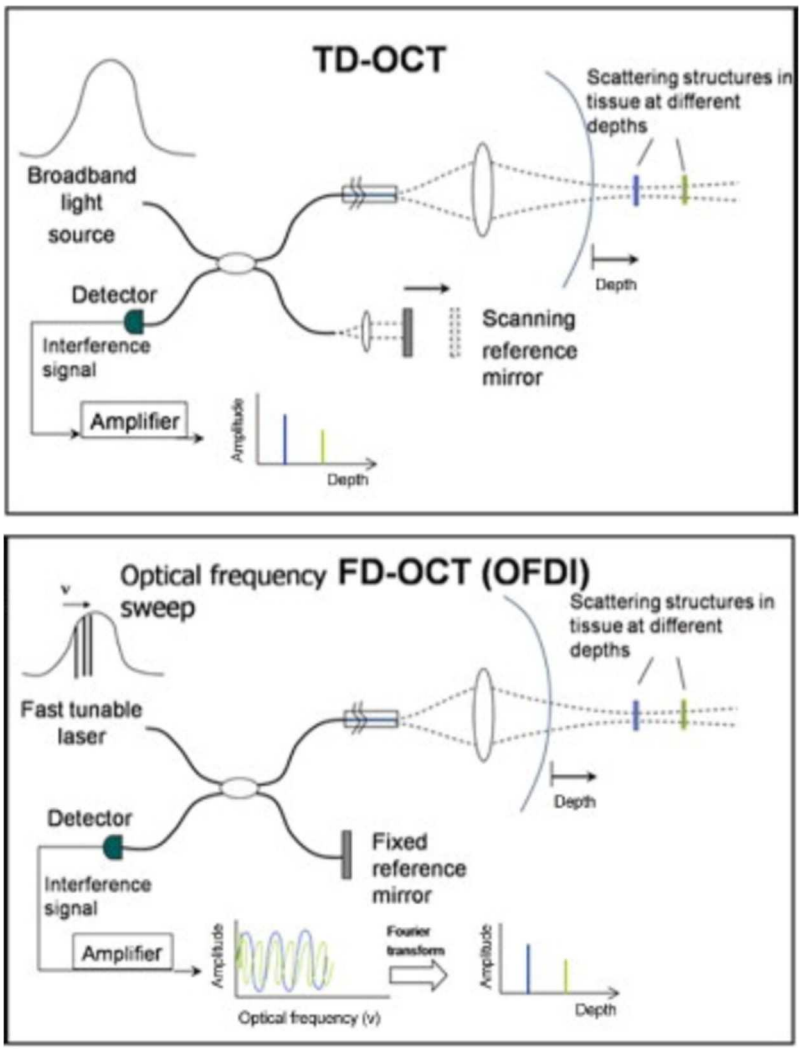

Figure 2.4 – Schematic representation of Time Domain OCT (TD-OCT) - on the top panel - and Frequency Domain OCT (FD-OCT) – specifically a subtype called Optical Frequency Domain Imaging (OFDI OCT) - on the bottom panel. Image source: [11].

A recent development is the Polarization Sensitive OCT that uses polarized light to evaluate the birefringent[12] and specific optical rotation of the eye globe's different tissues, allowing a better discrimination between them.

The technique used for the acquisition of the analyzed images is a variant of the Frequency Domain OCT called EDI-OCT[13]. In this method, the OCT device is moved closer to the eye, making the focal plane (zero-phase delay) close to the choroid, resulting in a better resolution in the deepest regions. To deal with the random noise, every A-scan is a result of an average of 100 scans.

The changes in the position of the focal plane create a visible reflection in the OCT image, as shown in Figure 2.5, that otherwise would occur out of bounds. In this image, the reflection is more visible in the scleral area, not influencing the choroidal segmentation.

The advances in the OCT technology allow it to become a more useful tool in the medical imaging department and contribute to the health of millions of people's eyesight.

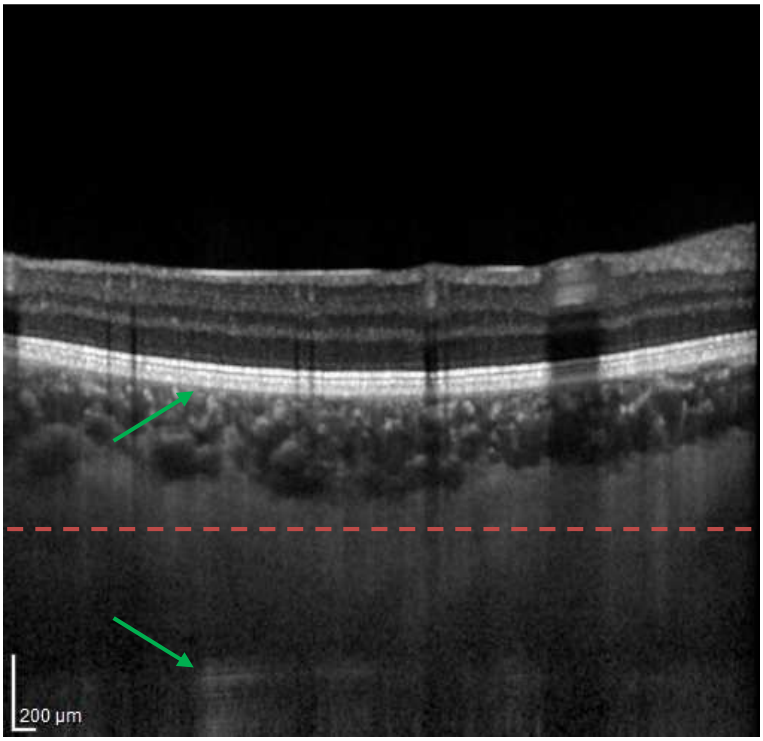

Figure 2.5 – EDI-OCT image of the human eye globe. The green arrows represent a layer of the retina and its projected reflection. The red dashed line is the probable focal plane.

2.3 - Choroidal Thickness Measurement

There are several recent studies that try to tackle the issue of automatically segmenting the choroid. In this section, the relevant articles for the development of this work will be cited and explained. The articles will be distributed according to the main method applied for the segmentation and their analysis is subdivided in three main parts: preprocessing, segmentation of the choroid and evaluation measurements of the obtained results.

The preprocessing part includes all the steps that modify the image in order to improve the results of other methodologies applied posteriorly. It can include filtering, noise reduction, region of interest selection, contrast adjustment, amongst others. The preprocessing is a relevant stage of this project because the OCT image has characteristics that can influence the final results. Speckle noise, shadows cast by retinal vessels and loss of intensity of the signal with depth are some of the adversities that can be managed by preprocessing algorithms.

The segmentation of the choroid is made essentially in two ways: by using classification methods with characteristics of the choroid or by delineating the inner and outer boundaries of the choroid with some kind of curve defining method.

The classification methods are based on the extraction of characteristics that may distinguish the choroid from the rest of the eye globe. With those characteristics, a classifier is trained to correctly segment other images' areas and identify as part of the choroid or other layer tissue.

The other type of segmentation is based on graph-based approach, for example, minimum cost path algorithm or active contour model. These algorithms try to fit a line to the choroidal boundaries, using the image's properties. The first layer to locate is usually the ICB that corresponds to the BM. It has a simple shape and is closer to the retina, where the OCT signal is more intense (the light has to penetrate less layers). The inner layer can also help with the location of the OCB that corresponds to the SCI.

The third part is the algorithm's evaluation, which enables the comparison between different approaches. Some articles' results are hard to compare because they use different evaluation criteria and different databases as well. In these cases, the evaluation can only be made individually invalidating any objective comparison to other methods.

Some papers, where the eye globe is segmented in OCT images, use methods that are not so similar to the one proposed for this work. Some use a semi-automatic approach [14], [15], others segment the retina but not the choroid [16]–[18] and others use Polarization Sensitive OCT technique that involves a new dimension of data, influencing the type of characteristics used in the segmentation of the choroid [12], [19].

Graph-based segmentation

Graph-based strategies use the Dijkstra's algorithm as a method to calculate the lowest cost path between two predefined initial and final nodes. The requirements for the algorithm are the path nodes (candidates to be part of the connection) and the costs of the possible paths between the nodes.

Preprocessing

Alonso-Caneiro's[20] preprocessing initiates by normalizing the image, when each A-scan is divided by its maximum. This normalization helps minimizing the effects of the shadows cast by retinal vessels. To further enhance the ICB, values lower than 75% of the maximum are multiplied by 0.8. To deal with the speckle present in the OCT images, a rectangular average filter, sized 5×22 pixels, is applied to the normalized image, smoothing it.

J. Tian[21] chooses a different approach: initially the thermal and electronic noise was reduced by filtering the image with a 5×5 Wiener filter, which is adaptive to the existing noise

level. For the speckle noise, a moving average filter is used in each A-scan, but there is no specification on the size of the linear kernel.

Segmentation

The first step of the segmentation, is to locate the ICB. Both Alonso-Caneiro[20] and J. Tian[21] starts by detecting the close RPE layer. The detection method takes advantage of the layer's high reflective nature by selecting the highest values in every A-scan. After that, a vertical gradient filter is applied in order to show the variations of intensity in the distal direction. The highest gradient after the RPE is the BM that defines the ICB. J. Tian[21] fits a 4^{th} order polynomial function to the rough BM in order to smooth the contour.

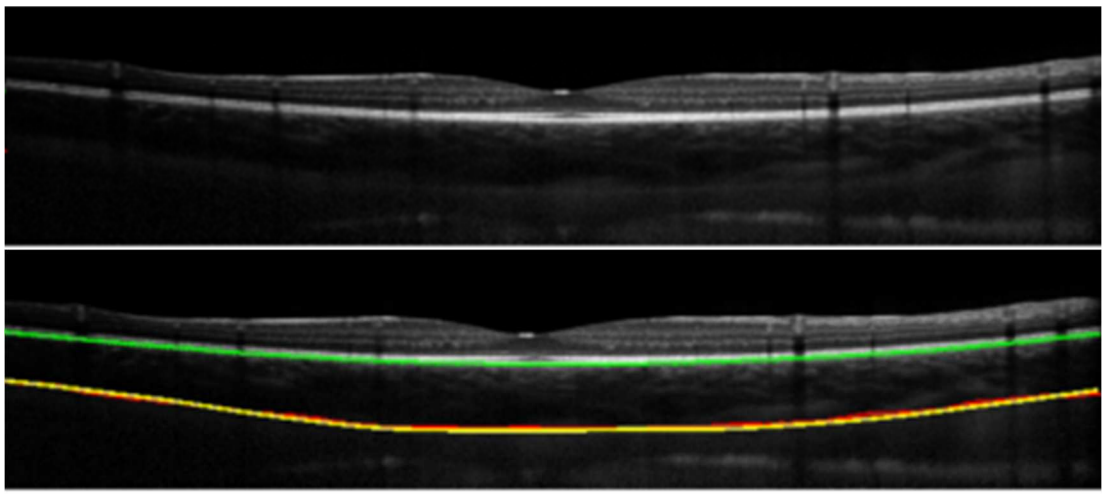

Figure 2.6 – On the top image, the original OCT B-scan. On the bottom, plotted in the OCT B-scan, the calculated inner and outer choroidal boundaries are shown in green and red, respectively whereas the yellow is the manual segmentation of the OCB. Adapted from [20].

The next step, in the two papers' methods, is to flatten and crop the B-scan according to the found BM, as shown in Figure 2.6. The flattening is useful because the search area becomes smaller and CSI becomes a flatter layer, approximating the shortest geometric path to the weighted path to be calculated. The flattening of the image is computed by translating each A-scan so that the ICB is positioned on the edge of the image. Alonso-Caneiro[20] crops a region of 565 microns below the ICB which corresponds to a height greater than twice the thickness of the average choroid (272±81μm)[5].

For the path search algorithm, the initial and end nodes are set as the lateral limits of the image and the connections to the closest nodes are assigned the minimal cost, so that the path goes from one side of the image to the other.

For the calculation of the OCB weight function, Alonso-Caneiro[20] starts by enhancing the OCB in the flattened image according to Girard[22]. Influenced by the processing of the ultrasound, Girard[22] proposed a contrast compensating algorithm that reduces the cast shadows and improves the quality of the signal in the deeper structures. The compensation algorithm was also applied to enhance the contrast using intensity-expansion techniques.

Contrast adjustment saturates 25% of the data (that should not be relevant) and a mask is applied, which multiplies each value in a row by its row number. This masking enhances the sclera, comparing to the choroidal dark vessels, delineating the OCB. A noise reducing average filter is then applied with a size of 2×22 to smooth the image.

Alonso-Caneiro[20] uses all the pixels of the processed image as vertices and the cost between them is defined by a weight matrix. This weight matrix is a function of a dual gradient boundary detector (based on Arbeláez[23]). This method involves the average of two gradients calculated in distinct ways. One is based on the intensity difference of two halves of a disc, where the orientation is given by the division of the disc. After that, a non-maximum suppression is applied on the orientation of interest, resulting in a selective but coarse boundary estimation. The second one is less selective; it is constructed from the multiplication of a Canny edge detection of the original image by the gradient in the vertical direction calculated in the other part of the method.

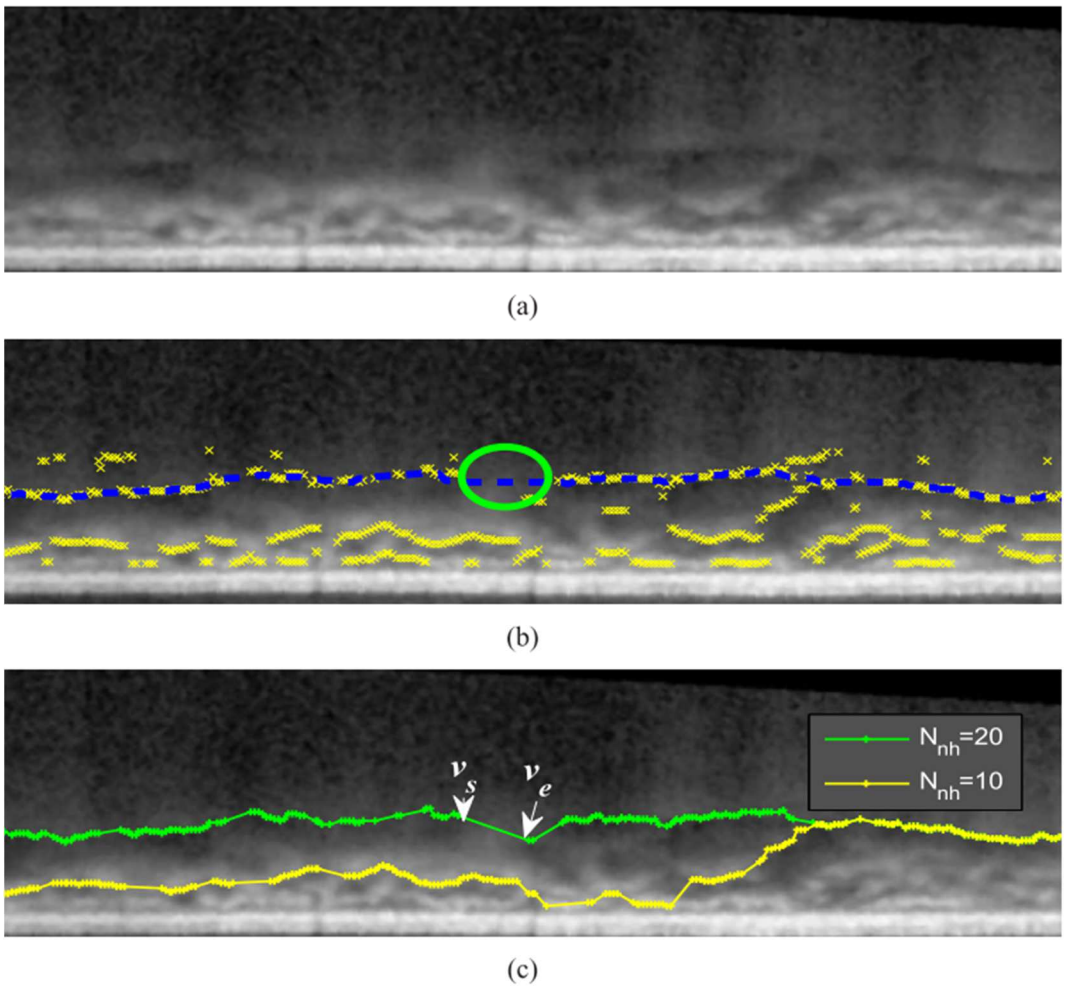

Figure 2.7 – (a) – Flattened and inverted OCT image (with the RPE appearing in the bottom of the image). (b) Yellow crosses represent the vertices for the construction of the graphs, blue dashed line is the manually labeled CSI and the green circle highlights the missing vertices in the CSI. (c) Example of what the modification of the horizontal range's value (N_{nh}) can modify in the resulting path –10 pixels do not cover the gap between the vertices v_s and v_e, so the yellow path is deviated from the correct one. Image source: [21].

Although the basic algorithm used by J. Tian[21] is the same (Dijkstra's minimum path algorithm), the approach is quite different. To determine the nodes for the path calculation, an algorithm selects the local minima of every A-scan, as represented in Figure 2.7(b). The local minima can be part of the CSI as well as vessels of the choroid or random noise of the OCT image. Graphs are then formed by sets of vectors that connect one local minima to others within vertical and horizontal range (set as 30 and 25 respectively). As exemplified in Figure 2.7(c), a fine tuning of this range's size is important because big ranges can lead to deviations of the detected OCB to choroidal textures and smaller ranges can create unnatural jumps between closely connected vertices and errors in the final detection. The cost of the path to be assigned in the Dijkstra's algorithm in this case is the weighted distance between the vertices based on a Heaviside function.

Evaluation

To evaluate the results obtained, Alonso-Caneiro[20] calculates the mean absolute and signed errors (with standard deviations) of the detected boundaries to the manual outlined ones and compares them to the errors of repeatability of the manual segmentations made by the same person. The Dice coefficient (ratio between two times the area of intersection and the sum of the areas of the detected choroid and ground truth) is usedto evaluate segmentation and compare results with those published by J. Tian[21]. To evaluate repeatability and correspondence to the manual segmentation the correlation between the two methods was also computed.

J. Tian[21] evaluated his results using Dice's coefficient and correlation coefficient between the average manual segmentation and the automated one.

Segmentation by Classification Techniques

Three papers [24]–[26] were considered in this section, as they apply strategies of feature extraction. However, the features used, the methods of extraction and the way the data is manipulated varies between the three papers.

Preprocessing

The pre-processing in these papers includes the calculation of the initial boundaries as this phase is crucial for the preparation for feature extraction and classification.

V. Kajić[24] starts by applying a dual-tree complex wavelet denoising, with the objective of reducing the speckle noise. The next step is to eliminate the non-signal areas which are identified using a Canny edge detection algorithm to locate the limits of the relevant data. Here the lowest cost path is found using Dijkstra's algorithm, where each pixel is a node for the path and the weight function is defined by the inverse of the intensity (as in the previously analysed paper). A cubic spline algorithm is applied to smooth the calculated RPE and the BM

is located by applying a second time the Dijkstra's algorithm to regions close to the previous boundary. However, this time the cost function is defined directly by the intensity of the image This paper also defines the internal limiting layer of the retina to distinguish it from the non-signal areas in the feature extraction algorithm.

In the article of H. Danesh[25], the first step is the location of the RPE using dynamic programming which finds the path of highest intensities. Dynamic programing is used as an algorithm to locate the lowest cost path between the image's lateral boundaries and the cost function is inversely proportional of the inverse of the intensity. The BM is then located by finding the more intense gradient below the RPE.

The initial process in the paper of A. González-López[26] is to locate the region of interest that defines the area of the choroid and sclera. The RPE is selected using an active contour algorithm described in another article from the same author[27], where the internal energy is defined by first and second degree terms to guarantee continuity of the curvature, and the external energy is a combination of the gradient distance function and the distance between the node and the strongest edge (RPE).

The last two papers do not mention any kind of noise reducing technique, which is normally recommended in the OCT images.

Segmentation

H. Danesh[25] uses the difference in texture between the vascularized choroid and the smooth sclera, using a four level discrete wavelet transform with a Haar wavelet.

The next step is to compute the discrete wavelet transform, whose coefficients give information about the image's texture. The features of the OCT image are extracted using a filter bank and the energy of the wavelet coefficients. A set of training images (previously segmented and with features extracted) is used for the construction of a Gaussian mixture model that results in a probability function to classify the test images. The comparison with this model allows the image's segmentation in three areas: the area above the BM (that was set to 0 after the boundary detection), the choroid and the area below the CSI. This segmentation allows the calculation of the choroid thickness and its boundaries, as illustrated in Figure 2.8.

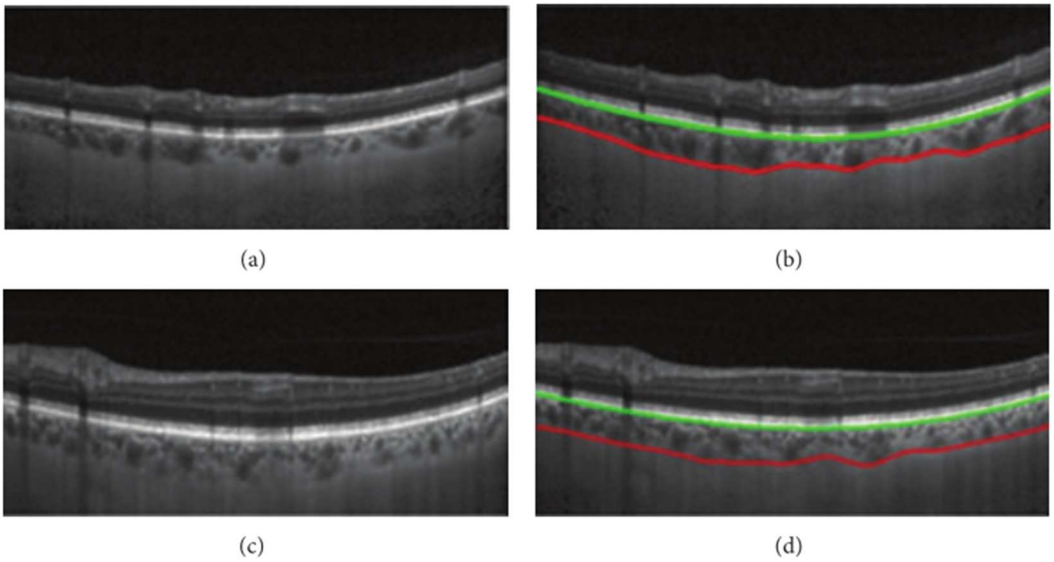

Figure 2.8 – Two examples of the results obtained using the method by H. Danesh. The left image is the original one and in the right the BM boundary is represented in green and the CSI in red. Image source: [25].

V. Kajić[24] uses a statistical model to segment the choroid from the OCT data. The BM's and CSI's features are extracted from the training images; these are composed by shape features of 26 points in each boundary. Principal Component Analysis is made lowering the dimensions in the datasets, reducing the computational cost of the classification and avoiding errors in the segmentation due to meaningless features. Classification uses this matrix of characteristics of the train set for the comparison with the features of the different areas in the image. An example of a obtained result is represented in Figure 2.9.

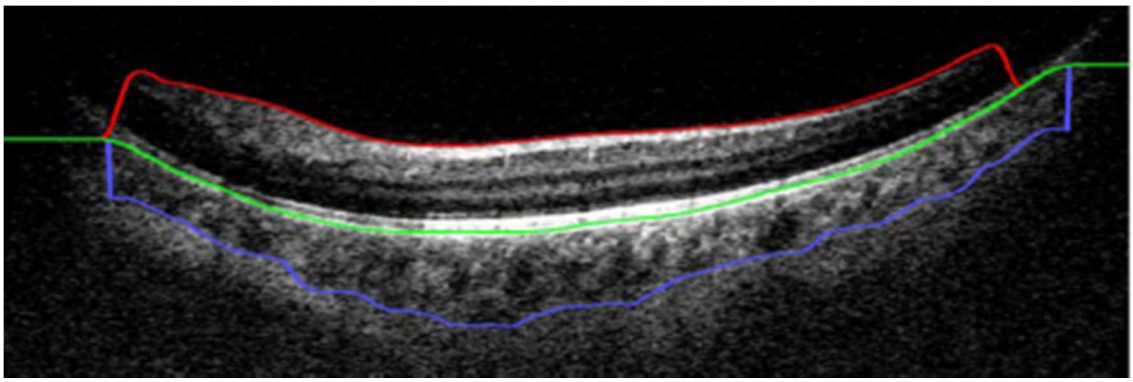

Figure 2.9 – Result obtained by V. Kajić in a typical diabetes type 1 eye, where the estimated boundaries are presented: internal limiting layer (red), BM (green) and CSI (blue). Adapted from [24].

The features that A. González-López[26] extracts to be able to segment the choroid are based on three algorithms: Markov random fields, co-occurrence features and the discrete wavelet transform (to allow a comparison to H. Danesh[25]). To use Markov random fields, the selected features are the grey levels of a neighbourhood and the directional variances on it.

These captured features are selected by the author as the best to distinguish the choroidal layers. Co-occurrence features are based on the Grey Level Co-occurrence Matrix that counts the different types of transitions existent in the image for a particular direction (in these case 0º, 45º, 90º and 135º). These features can define characteristics of the texture, such as homogeneity or contrast and, for this paper, 14 were selected and represented as a mean and range (28 in total). The discrete wavelet transform consists in decomposing an image using a high-pass filter (H) and low-pass filter (L) using wavelets in both vertical and horizontal directions, originating 4 new subsampled images (LL, LH, HL and HH). The process is then applied to the LL subimage iteratively, resulting in a pyramidal decomposition of the image. The final features to use in the classifier are the mean and standard deviation of the input and LL subimage and the energy of every LH, HL and HH subimages.

A feature selection algorithm is applied to reduce the dimensions of the features and eliminate features that do not have real influence on the result. The classifier that segments the choroid is a Support Vector Machine which identifies characteristics in an N-dimensional hyperplane in a number of chosen categories.

Evaluation

The evaluation methods used by H. Danesh[25] were the calculation of the mean signed and unsigned errors of the located boundaries, and their comparison to the errors of different methods as graph cut, k-means (k=3), dynamic programming. The differences between the two sets of manual segmented boundaries were used as a reference for the error calculation.

In V. Kajić's paper[24], only the absolute error and the Dice coefficient are used to evaluate the deviations of the boundaries and the segmented area from the ground truth.

A. González-López[26] uses the accuracy of the classification to evaluate the 3 tested techniques. The best results were obtained when using the co-occurrence features of characterising transitions with a distance of 3 pixels. The best option in the other techniques was, in the Markov fields, a neighbourhood distance of 1 pixel, and in the discrete wavelet transform the best accuracy was achieved by using a 2 level decomposition with the Haar wavelet.

3D segmentation techniques

Modern OCT equipment can obtain 3D OCT of the eye which opens new possibilities to process the data. The use of a volumetric data allows the segmentation of the vessel net in the choroid which, in a B-scan (two dimensional OCT), appears sectioned with a variety of shapes.

Li Zhang's paper[28] is a relevant paper that deals with 3D images but does calculate the thickness of the choroid, instead of just segmenting its vessels.

Preprocessing

The first step of the preprocessing is to search for the BM surface that limits the choroid by using a multi-layer, graph-search based segmentation approach[29]. Then, the volume is flattened according to the BM and cropped to a sufficiently thick region below it, as seen in the other papers and illustrated in Figure 2.10. To remove the effects that shadows can have in the OCT's deeper regions, Li Zhang[28] introduces a three stage method to deal with it and prevent bad vessel segmentation, by adjusting the regions contrast. The first stage is the definition of the RPE layer. The second stage is the formation of a projection from the average of the values of A-scans in the RPE. This is only possible since the layer is three dimensional (has a small thickness). The cast shadows are then segmented[30] in this projection, identifying the regions they affected. The final stage is to build a mask based on the shadows found, in order to increase the intensities of the shadows and minimize the transitions caused by them.

Segmentation

The choroidal vessels are then segmented based on the fact that the vessels are tubes (only possible using volumetric information). To do this, a multiscale Hessian matrix is applied and the eigenvectors of the tensor matrix analysed to calculate a vesselness map. On this map, the higher values are selected and a region growing algorithm is applied do select the whole portion of the vessels.

Having the vessels segmented, the CSI is defined using a thin plate spline algorithm on the choroidal vessels' voxels more distant from the retina. The choroidal thickness is then defined as the distance, in each A-scan, between the CSI and BM layers, as illustrated in Figure 2.10(D).

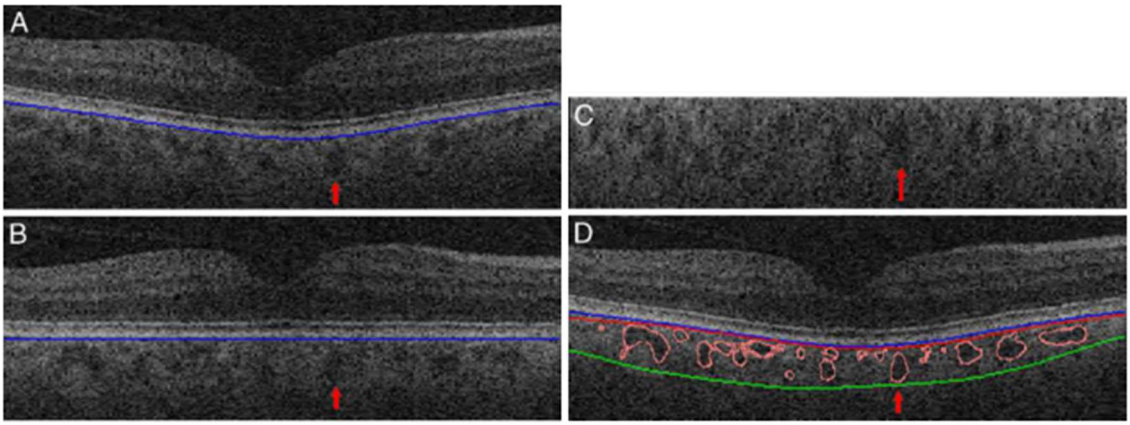

Figure 2.10 – Central B-scan selected from the 3D data. (A) Original OCT B-scan with a plot of the segmented BM (blue line). (B) OCT B-scan, flattened according to the segmented BM. (C) Cropped and flattened image where the vessels were segmented, containing the choroid. (D) Original OCT image with the correspondent segmented vessels (pink lines), segmented BM (blue line), and top (purple) and bottom (green) membranes sections fitted around the choroidal vasculature to determine choroidal thickness and choriocapillaris-equivalent thickness. The red arrow is pointing to the same vessel in all images. Image source: [28].

Evaluation

The values calculated in article[28] to evaluate the results are the overlapping rate, the skeletonized overlapping rate and the Dice Coefficient, however they are only applied to the segmented vasculature and not to the segmented choroidal layer or boundaries. To further evaluate the used methods, another paper[31] was published to validate the obtained results. In this revision article they analyse the absolute and relative errors between the automatic segmentation of the boundaries and two manually segmented boundaries in the central B-scans of each volumetric image. Other values like the 95% limit of agreement and the 95% confidence interval are calculated and analysed. To evaluate possible systematic bias in the automated algorithm, a t-test is also performed on the error results.

Chapter 3

2D Choroidal Segmentation

3.1 - Overview

The approach for the choroidal segmentation (that will enable the calculation of its thickness) was to locate the inner and outer boundaries of the choroid. As described in the previous chapter, these boundaries are the BM and the CSI. Because the innermost parts of the OCT normally have a better signal to noise ratio, the algorithm starts by processing the inner paths (BM) and detects the CSI afterwards.

In Figure 3.1, a schema of the proposed algorithm for choroidal segmentation is represented. It starts by selecting the B-scans from the initially acquired videos. In this step, the video frames are automatically cropped to exclude irrelevant data (as the legend and location information) from every B-scan. The following step is the intensity adjustment where the OCT image is returned to its raw format[20].

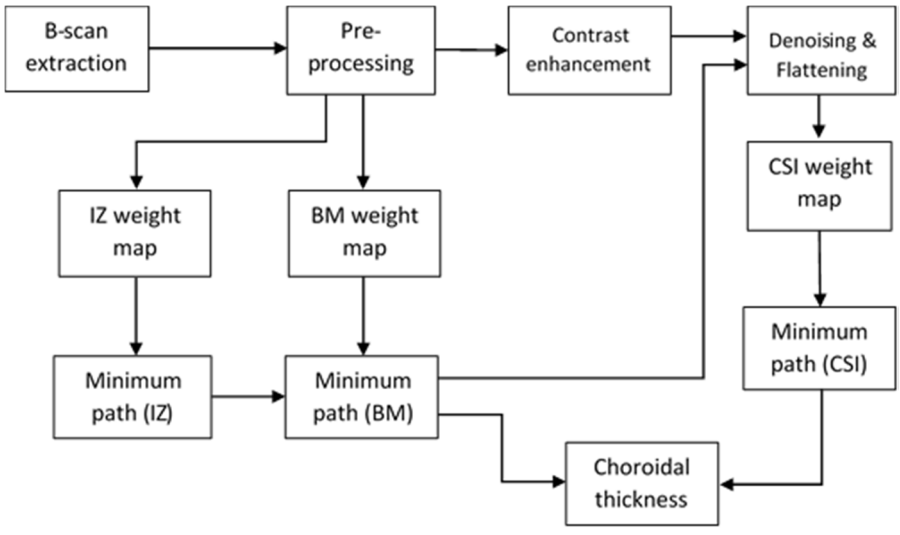

Figure 3.1 – Diagram representing the process of the choroidal segmentation and the measurement of its thickness.

In the obtained raw image, the highest values have a better contrast which helps the detection of the brightest layers of the OCT. As a precursor for the BM's delineation, the IZ is estimated. It is the middle layer of the three brightest of the OCT, marked in green in Figure 3.2. The IZ is found by running a minimum path algorithm. This algorithm was developed as a dynamic programming method whose input is a selected weight matrix.

The vertical distance to this initial layer serves as a parameter for the weight map of the BM (used for the definition of the weights in the minimum cost path algorithm) together with a vertical derivative of the OCT. The result of the minimum path can be seen in orange in Figure 3.2.

In the contrast enhancement step, a compensation algorithm is used to intensify the contrast in the OCT's deepest regions (external layers of the eye), making the CSI more easily detected.

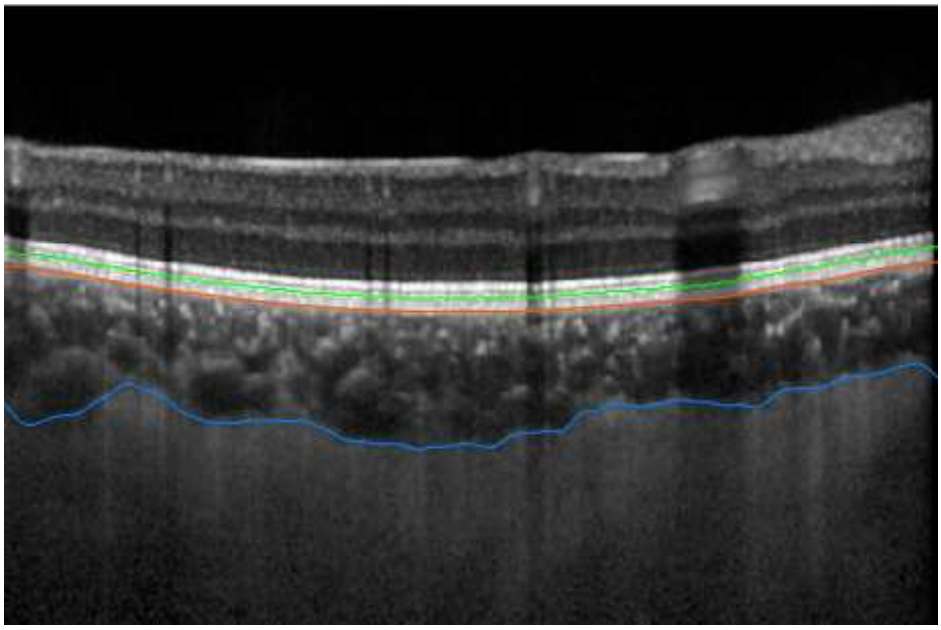

Figure 3.2 – B-scan of the OCT with plots of the three detected layers. The IZ estimation is represented in green, BM is outlined in orange and, in blue, the CSI. The choroid is delimited by the two last layers, BM and CSI.

In order to flatten the OCT, the BM is used as reference and a region (that includes the choroid) is selected below the BM. The denoising is made using a wavelet transform, making the shadows less pronounced and reducing the speckle noise in the deeper layers.

For the choroidal outer limit (CSI), the minimum path algorithm is run with a weight map, based on two derivative filters. The blue line in Figure 3.2 represents the detected CSI boundary.

Once the choroid is segmented, the choroidal thickness is calculated by averaging the vertical distance between the two limiting boundaries.

3.2 - Preprocessing

The extracted sets of OCT images, acquired by a Heidelberg Spectralis equipment, were saved in a video format. This video, as illustrated by the frame in Figure 3.3, in addition to the B-scans, has a caption, axes, markings and a corresponding fundus image - or Infrared Reflectance (IR) image - that helps with the location of the B-scan in the eye. To select only the B-scans of each frame, the B-scan edges are calculated according to the transitions present in the vertical and horizontal projections of the images. These projections allow an easy detection of the limits between the two images and the background. The vertical projection (sum of the pixels in each column) is used to detect the left border of the B-scan and the horizontal projection (sum of the pixels in each row) for the top and bottom ones.

Figure 3.3 – Example of a frame of the original OCT video.

The Heidelberg Spectralis processes the B-scans to provide a better visualization of the darker layers[20]. Because the first layers to detect are the brightest, the contrast is adjusted by reverting the B-scans to the raw format $\boldsymbol{I_{raw}}$ visible in Figure 3.4(b). To revert the images, every pixel in the B-scans $\boldsymbol{I}(i,j)$ are raised to the fourth power [20] as in Equation (3.1) (where i and j are the images' coordinates).

$$\boldsymbol{I_{raw}}(i,j) = \boldsymbol{I}(i,j)^4 \tag{3.1}$$

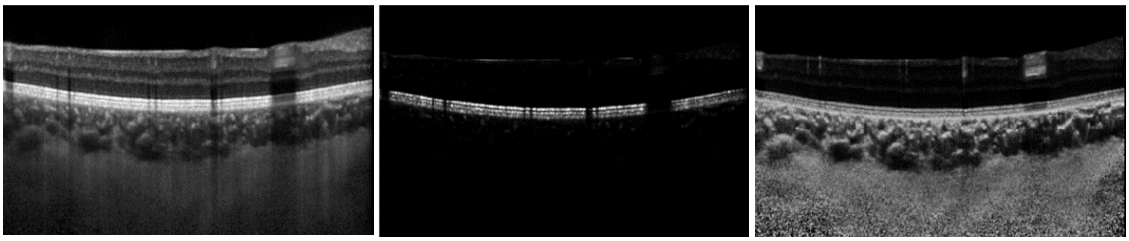

(a) (b) (c)

Figure 3.4 – (a) Original cropped OCT B-scan; (b) Raw form of the OCT B-scan; (c) Contrast compensated OCT B-scan.

Following the intensity transformation, a contrast compensation method (proposed in [22]) is used to attenuate the loss of energy in the deepest layers, caused by the scattering of light in the tissues above. The compensation method is based in the formula expressed in Equation (3.2).

$$\boldsymbol{I_{comp}}(i,j) = \sqrt[4]{\frac{\boldsymbol{I_{raw}}(i,j)^n}{2\sum_{k=i}^{H}\boldsymbol{I_{raw}}(k,j)^n + \varepsilon}} \tag{3.2}$$

In the previous equation, i and j are the line and column of each pixel in the B-scan image, H is the height of the B-scan (or the maximum i), ε is an infinitesimal positive value to avoid the division by zero. The exponentiation factor n was set as 2 (as proposed in [20]); this factor contributes to enhance the contrast between tissues.

This compensation (Equation (3.2)), deals with the shadows created by the retinal vessels, projected to the choroid, and enhances the contrast in the region of the CSI. The high gain in the deep tissues also makes the speckle noise more intense, as observable in the scleral region of Figure 3.4(c).

To facilitate the delineation of the CSI, the BM's position is taken as a reference to flatten the B-scan and a more restricted area is selected. This process is performed in order to enable a horizontal smoothing to reduce the noise without hindering the transitions between the choroid and sclera (that become mainly vertical or diagonal after the flattening). The flattening is applied by considering each pixel of the BM as the first of its column[20] and moving each column accordingly. The height of the image is cut to 515 μm below the BM where the whole choroid should be present. The value of 515 μm was set because it corresponds to the value three standard deviations above the mean, considering the distribution values of 272±81μm [5]. An example of a flattened B-scan is present in Figure 3.6(b). All measures expressed in microns along this document are converted into pixels using the vertical and horizontal resolutions of the B-scan, as expressed in Chapter 5, this measures are inputs of the software system. The resolutions are expressed in the original DICOM images, in the equipment's characteristics or the axes present in the video frames.

After the area selection, the image is smoothed. To deal with some of the speckle noise but avoiding the reduction of the vertical details, important for the detection of the CSI, the smoothing function was based on the two dimensional Stationary Wavelet Transform (SWT). The SWT decomposition is schematized in Figure 3.5, where one can observe that, for each level of decomposition, an image is low-pass and high-pass filtered in two directions, originating the details' coefficients in the horizontal, vertical and diagonal directions and an approximation matrix that can be used for further decomposition. The difference between each level is the size of the low-pass and high-pass filters used. From one level to another, the filters are upsampled in order to have the double of the samples they had before, as schematized in Figure 3.5; this is achieved by inserting zeros between every sample.

The difference between this SWT and the discrete wavelet transform is that, this last one, has a translation invariance associated with the downsampling of the image, which occurs in every level of decomposition (and not the upsampling of the filters).

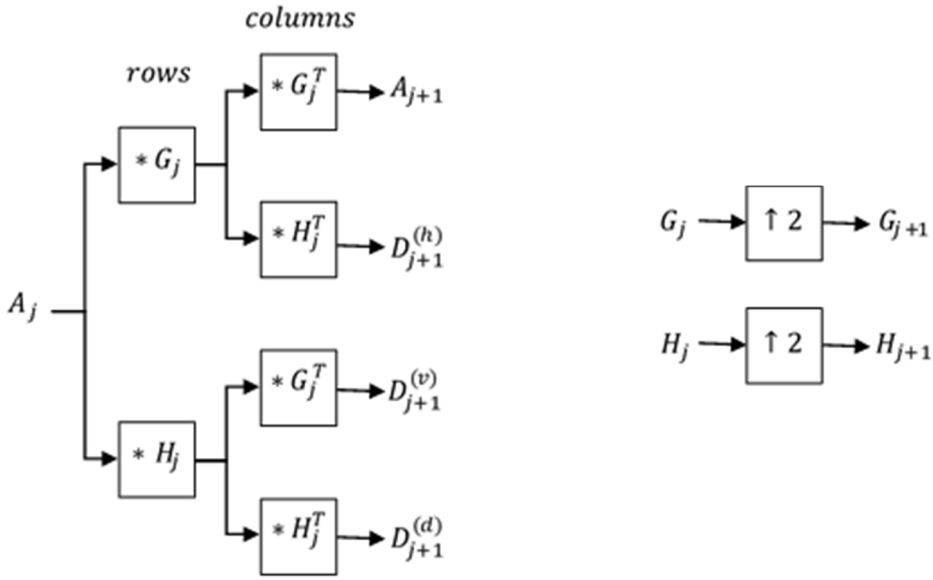

Figure 3.5 – Schema of SWT decomposition. A_j is a matrix with approximation coefficients at level j of decomposition (A_0 is the input image); $D_j^{(x)}$ is a matrix with the details coefficients at level j,with the direction defined by (x) (horizontal, vertical or diagonal); G_j and H_j are the low-pass and high-pass filters used in level j formed by a chosen wavelet, the filters are different in each level of decomposition because they suffer an upsampling ($\uparrow 2$) for each level.

In this case, the decomposition filters are formed with a Haar wavelet (the main referenced wavelet used for choroidal descriptors [25], [26]) and the maximum level of decomposition is 5, resulting in 15 matrices of details coefficients and 5 approximation matrices, all with the size of the original image.

The coefficients are then selected by a hard threshold according to the direction they represent. The vertical and diagonal coefficients remain unchanged, while the horizontal ones are set to zeros. This coefficient selection is made in order to maintain the transitions between

choroid and sclera while reducing the noise intensity and textures inside the choroid. The image is then reconstructed with the selected coefficients, becoming as exemplified in Figure 3.6(c).

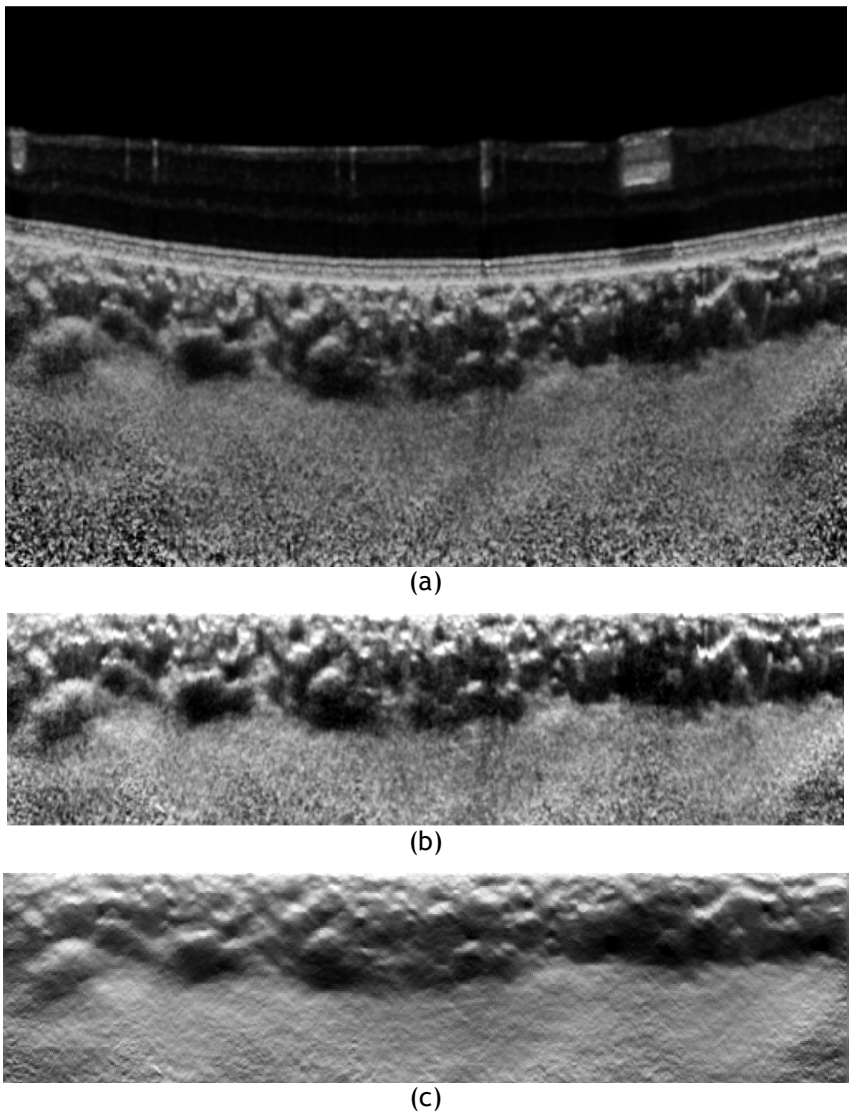

Figure 3.6 – (a) - B-scan after contrast compensation; (b) – Contrast compensated B-scan after flattening and cropping; (c) – Flattened B-scan after wavelet based denoising.

3.3 - Minimum path algorithm

The objective of a minimum path algorithm is to find the path with the minimum cost from the initial node to the last, according to a weight function that defines the cost of all the existent connections between nodes. The initial approach was to apply Dijkstra's algorithm to search the choroidal limits in the OCT, as proposed in literature[20]. However, an analysis of the behavior of the paths that define the choroidal limits, allowed the establishment of some constrictions that tremendously reduced the path search time. This time saving is explained by the smaller number of cycles the program needs to execute, in order to calculate the costs to

reach the final node. Consequently, the algorithm can be used three times in the overall choroidal segmentation methodology (to estimate the IZ, the BM and CSI).

Because the images used in this work have the choroid reaching both B-scan's lateral edges, the initial and final nodes are set outside the left and right edges of the image, as represented in Figure 3.7(a), connected to every pixel of the first and last row. In this way, there is an assurance that the path crosses the whole B-scan without imposing restrictions to the path's rows. These initial and final nodes are not part of the final boundary.

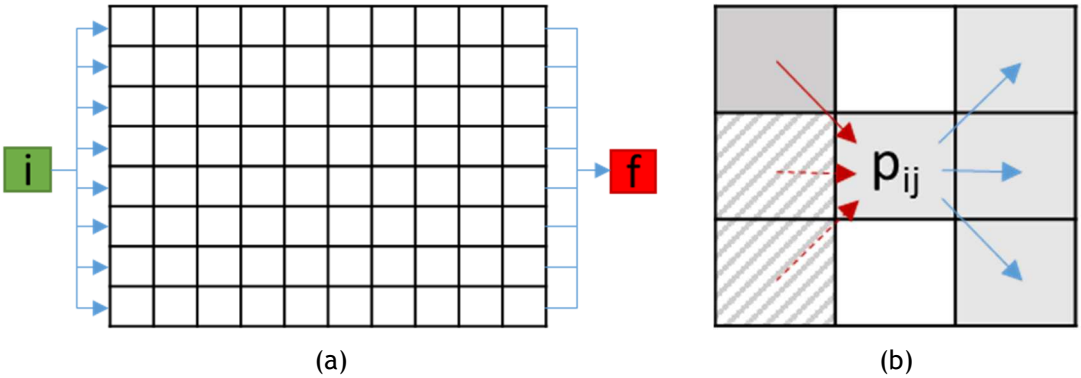

Figure 3.7 – Illustrative schema of the conditions of the nodes that will represent paths in an image (a) definition of initial, i, and final, f, nodes; (b) node connectivity.

The other intermediate nodes that form all possible paths are the B-scan's pixels and each one of them is restricted to be connected to the 3 closest pixels in the next column as represented in Figure 3.7(b). This restriction prevents the path from assuming unnatural tortuous directions, making it go forward to one of the neighboring nodes (since the image was flattened there are not major deviations from the horizontal directions).

These restrictions to the algorithm also allow the path search to be progressively made, column by column, by finding the minimum cost of the paths (C) until the 3 previous nodes and add the weight value ($\boldsymbol{W}(i,j)$) of the current node, as represented in Equation (3.3).This restriction exempts the need for the search of the minimum path in the whole image (as necessary in Dijkstra's algorithm).

$$\boldsymbol{C}(i,j) = \min\big(\boldsymbol{C}(i-1,j-1), \boldsymbol{C}(i-1,j), \boldsymbol{C}(i-1,j+1)\big) + \boldsymbol{W}(i,j) \tag{3.3}$$

When the algorithm reaches the final node, a search is made in the last column (L) to find the lowest path cost ($Cpath$), as represented in Equation (3.4), and define the first node that forms the boundary.

$$Cpath = \min(\boldsymbol{C}(L, j)) \tag{3.4}$$

To recall the line indices of the path for each column, a back search from the last selected node is made. A new node is selected to form the boundary if it is the one with the least weight and is connected to a previously selected node.

The weight functions are defined from the B-scans, by using processing operations specific for each path (IZ layer, the BM or CSI). The specific weight matrices used in this methodology are defined in the next section.

3.4 - Weight matrices

Throughout the methodology for the segmentation of the choroid, the minimum cost path selection algorithm is run three times for each B-scan, one for each estimation of the three limiting membranes: IZ, BM and CSI. Every run is performed using a different weight matrix due to the different characteristics of the eye structure to delineate.

The first time this algorithm is used is to get an estimate of the IZ, the middle layer of the group of three brightest layers (inner/outer segment, IZ and RPE) located in the deepest part of the retina. Its estimate is relatively simple since the weight matrix ($\boldsymbol{W_{IZ}}$) will be a function of the arithmetic average filtered raw B-scan, as defined in Equation (3.5).

$$\boldsymbol{W_{IZ}} = 1 - \boldsymbol{J} * \boldsymbol{I_{raw}} \tag{3.5}$$

This average filtering is run with a 60 by 55 μm kernel ($\boldsymbol{J}$), because the thickness of these 3 layers in a healthy eye is approximately 60 μm. Due to this filtering, the final matrix has a weight valley around the middle of the 3 layers where the path is present, as visible in Figure 3.8 (b).

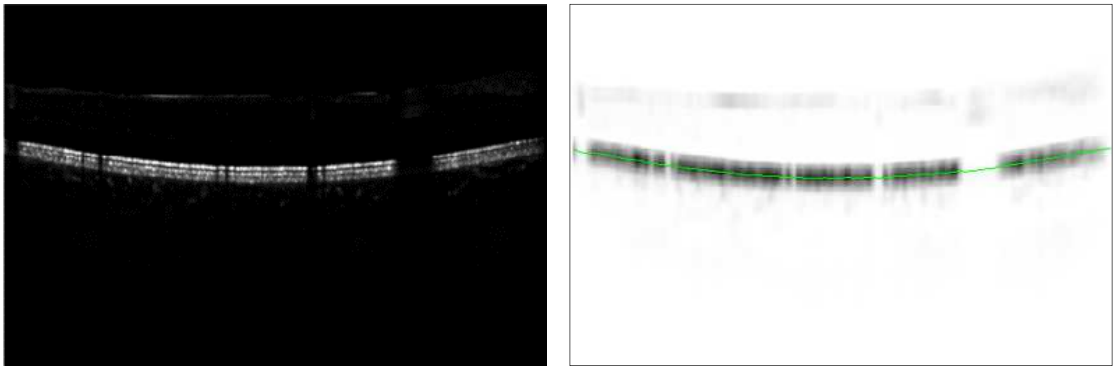

(a) (b)

Figure 3.8 – (a) $\boldsymbol{I_{raw}}$**:** image used for the calculation of $\boldsymbol{W_{IZ}}$ (b) Image representation of the weight matrix of the IZ layer $\boldsymbol{W_{IZ}}$ with the plot of the minimum path (estimated IZ layer) in green.

The weight function used for the BM detection ($\boldsymbol{W_{BM}}$) is calculated with a combination of two factors, the vertical distance to the estimated IZ and a cubed Sobel vertical derivative of the raw B-scan. These two factors were experimentally set and chosen because they generate good final results. Equations (3.6) to (3.8) detail the operations done to calculate $\boldsymbol{W_{BM}}$, and Figure 3.9(b) is an example of a weight matrix for the BM.

$$\boldsymbol{D_S} = \begin{cases} \boldsymbol{S} * \boldsymbol{I_{raw}}, & \boldsymbol{S} * \boldsymbol{I_{raw}} \geq 0 \\ 0, & \boldsymbol{S} * \boldsymbol{I_{raw}} < 0 \end{cases}, \qquad \boldsymbol{S} = \frac{1}{4} \times \begin{bmatrix} 1 & 2 & 1 \\ 0 & 0 & 0 \\ -1 & -2 & -1 \end{bmatrix} \tag{3.6}$$

$$\boldsymbol{L}(i,j) = \begin{cases} (\boldsymbol{IZ}(j) - i) \times \lambda, & \boldsymbol{IZ}(j) \geq i \\ 10, & \boldsymbol{IZ}(j) < i \end{cases} \tag{3.7}$$

In Equation (3.7), λ is a scaling factor equal to 1.2×10^{-3} times the depth resolution (vertical resolution of the B-scan) while $\boldsymbol{IZ}(j)$ is the ordinate of the IZ path for the column j; (i,j) are the line and column of a pixel in $\boldsymbol{L}$ according to the B-scan's axes. The distance factor has little influence in the calculation of the weight function, whose objective is to guide the path where the derivate is smaller (for example, where there is a shadow propagation) but it should not deviate the BM detection where the derivate is well defined. Forcing high values for the pixels above the IZ avoids deviations of the BM path to the dark places between the higher intensity layers.

Equation (3.8) is the formula that defines $\boldsymbol{W_{BM}}$, the weight matrix for the estimation of BM.

$$\boldsymbol{W_{BM}} = 1 - \boldsymbol{D_S}^{\circ 3} + \boldsymbol{J} * \boldsymbol{L} \tag{3.8}$$

$\boldsymbol{J}$ is a 60 by 170 µm kernel of arithmetic average and $\boldsymbol{D_S}^{\circ 3}$ is the third Hadamard Power of the matrix $\boldsymbol{D_S}$, where the power function is applied individually to every matrix element.

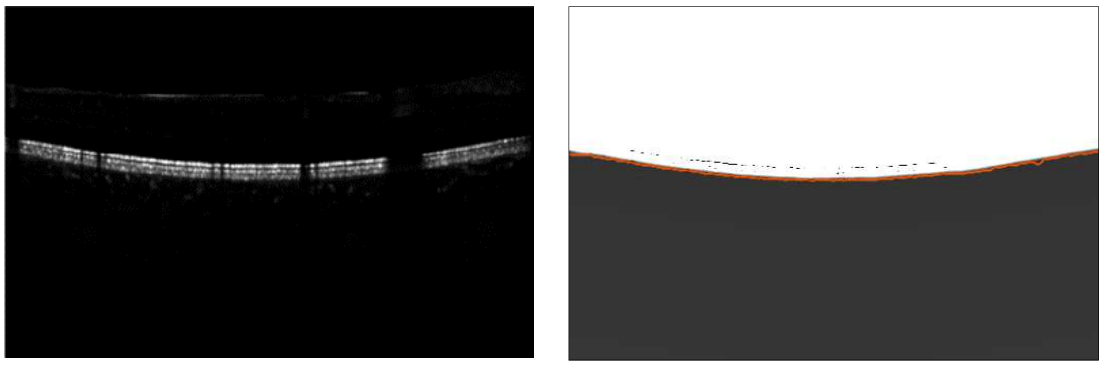

(a) (b)

Figure 3.9 – (a) $\boldsymbol{I_{raw}}$**:** image used for the calculation of $\boldsymbol{W_{BM}}$ (b) Image representation of the weight matrix of the BM layer $\boldsymbol{W_{BM}}$ with the plot of the minimum path (determined BM layer without further processing) in orange.

For the CSI, the weight matrix is a combination of two derivatives that mainly differ in the sizes of the kernels, allowing the weights to be a function of both high and low frequency information of the image.

These kernels are based on the derivative of a one dimensional Gaussian function.

The function expressed in Equation (3.9) is a defined integral in σ of the x derivative of the Gaussian function. In this equation, $G(\sigma, x)$ is the Gaussian function with a 0 mean, standard deviation σ and the abscissa x.

$$D(\sigma_{min}, \sigma_{max}, x) = \int_{\sigma_{min}}^{\sigma_{max}} -\frac{d}{dx} G(\sigma, x)\, d\sigma \tag{3.9}$$

As seen in Equation (3.10), the kernels are two dimensional because they are the result of a cross multiplication between the derivative function applied to a vertical vector and a horizontal vector of ones.

$$\boldsymbol{K}_n = D(\sigma_{n\_a}, \sigma_{n\_b}, \boldsymbol{x}) \times \boldsymbol{v} \tag{3.10}$$

$\boldsymbol{K}_n$ is the kernel to use in the flattened B-scan, where n is either 1 or 2. $\sigma_{n\_a}, \sigma_{n\_b}$ are two parameters that define the previous function; they either correspond to 48 and 80 µm if $n = 1$ or 12 and 40 µm if $n = 2$; $\boldsymbol{x}$ is a column vector centered in 0 with size $4(\sigma_{n\_a}+\sigma_{n\_b})$. Finally, $\boldsymbol{v}$ is a line vector with a length that corresponds to 55 µm.

Profiles of both kernels are represented in Figure 3.10 where the differences between them are visible, such as their range and values. Taking account the various sizes of vessels in the choroid, it is useful to apply a filter not limited to characteristics of a single size. These kernels allow a good adaptability to closer details without focusing on them too much - big vessels inside of the choroid could create similar responses if the kernel was too small.

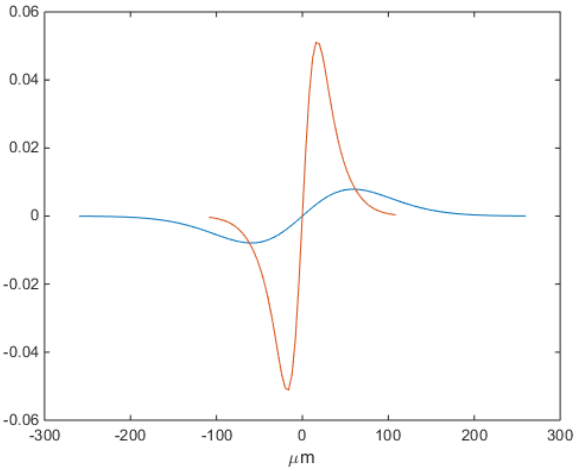

Figure 3.10 – Profiles of the derivative kernels ($\boldsymbol{K}_1$ in blue and $\boldsymbol{K}_2$ *in red*).

Equation (3.11) defines $\boldsymbol{D_1}$, the derivative matrix using the larger kernel $\boldsymbol{K_1}$. This matrix is defined as the filtered flattened B-scan (after an opening) if the result is higher than one, if that is not the case, the value is set as -1. $\boldsymbol{M}$ is the kernel used in the morphological opening consisting of a 80 by 100 μm matrix of ones applied to the flattened B-scan $\boldsymbol{I_{flat}}$.

$$\boldsymbol{D_1} = \begin{cases} \boldsymbol{K_1} * (\boldsymbol{I_{flat}} \circ \boldsymbol{M}), & \boldsymbol{K_1} * (\boldsymbol{I_{flat}} \circ \boldsymbol{M}) \geq 0 \\ -1, & \boldsymbol{K_1} * (\boldsymbol{I_{flat}} \circ \boldsymbol{M}) < 0 \end{cases} \tag{3.11}$$

Figure 3.11 shows a result of the morphological opening applied to a flattened B-scan. As visible in the figure, the open operation creates a dark choroid with much less detail and textural variance, useful for the determination of the CSI.

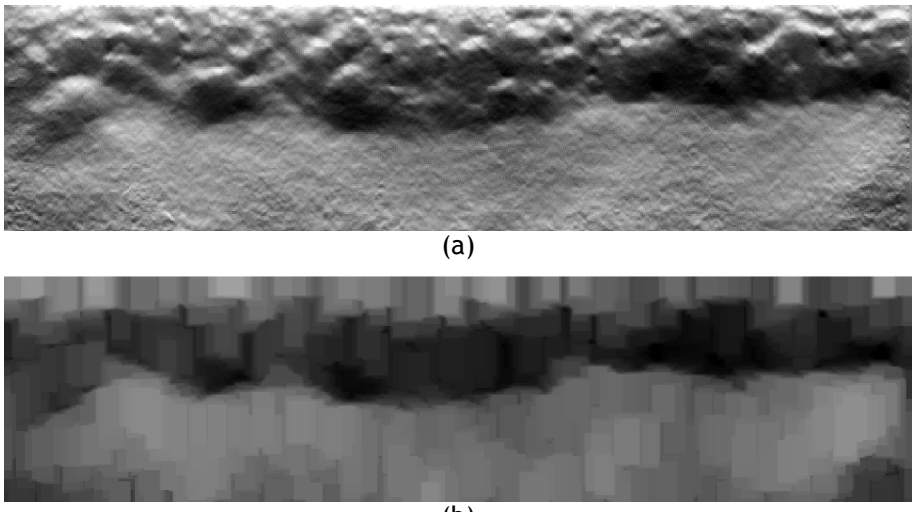

(a)

(b)

Figure 3.11 – (a) $\boldsymbol{I_{flat}}$**:** image input of the morphological open (b) Result of the morphological open of the B-scan, where the choroid contains less high values and less textures.

The differences between the definition of $\boldsymbol{D_1}$, represented in Equation (3.11), and $\boldsymbol{D_2}$, represented in Equation (3.12), are in the kernel used, the absence of an opening (avoiding the destruction of details) and the conditions under which the values are set to -1. In this case, the values are only defined as the result of the filtering when both matrixes $\boldsymbol{D_1}$ and $\boldsymbol{D_2}$ are positive.

$$\boldsymbol{D_2} = \begin{cases} \boldsymbol{K_2} * \boldsymbol{I_{flat}}, & \boldsymbol{K_2} * \boldsymbol{I_{flat}} \geq 0 \ \wedge \ \boldsymbol{D_1} \geq 0 \\ -1, & \boldsymbol{K_2} * \boldsymbol{I_{flat}} < 0 \ \vee \ \boldsymbol{D_1} < 0 \end{cases} \tag{3.12}$$

The final definition of the weight matrix for the delineation of the CSI, $\boldsymbol{W_{CSI}}$, is expressed in Equation (3.13).

$$\boldsymbol{W_{CSI}} = 2 - \boldsymbol{D_1} - \boldsymbol{D_2} \tag{3.13}$$

The weight function for CSI is simply dependant on the two modified derivative matrixes $\boldsymbol{D_1}$ and $\boldsymbol{D_2}$. The nodes' cost decreases with the intensity of the two matrices so that the CSI path is attracted to pixels with higher derivatives. An example of a weight matrix, $\boldsymbol{W_{CSI}}$, is represented in Figure 3.12 with the resulting curve obtained for the CSI.

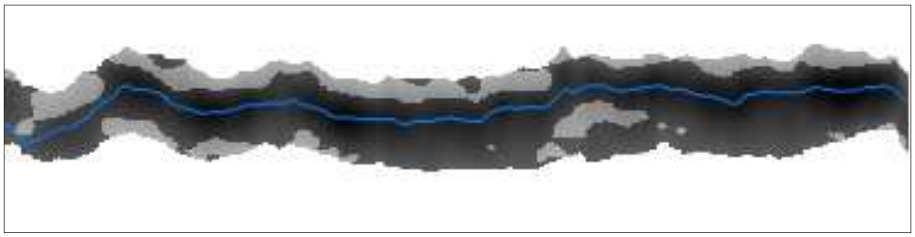

Figure 3.12 – Weight matrix to calculate the CSI, $\boldsymbol{W_{CSI}}$, and the plot, in blue, of the CSI boundary (without further processing).

3.5 - Choroidal thickness calculation

The choroidal thickness is defined, in the OCT image, as the vertical distance between the BM and the CSI. It can be measured in a single column or by averaging values calculated for a selected region.

To avoid the unnatural hard edges of the calculated boundaries, they are previously filtered. The two paths are filtered with FIR low pass filters designed using the Kaiser window method. The pass band normalized frequencies are .01 for the BM and .1 for the CSI while the stop band normalized frequencies are .1 and .2 respectively. The stop band attenuation was set to 60 dB for both filters. The filters have distinct frequencies due to the normal characteristics of the two boundaries, while the BM's topography is smoother, the CSI is influenced by vessels' tortuousness generating a higher frequency information.

Chapter 4

Merging sets of B-scans

4.1 - Overview

OCT's B-scans can be acquired vertically or horizontally, as illustrated in the examples in Figure 4.1. Sets of B-scans acquired in different directions usually need to be aligned to match the same locations of the eye as schematized in Figure 4.2. When aligned, a comparison between the two segmentations can be done.

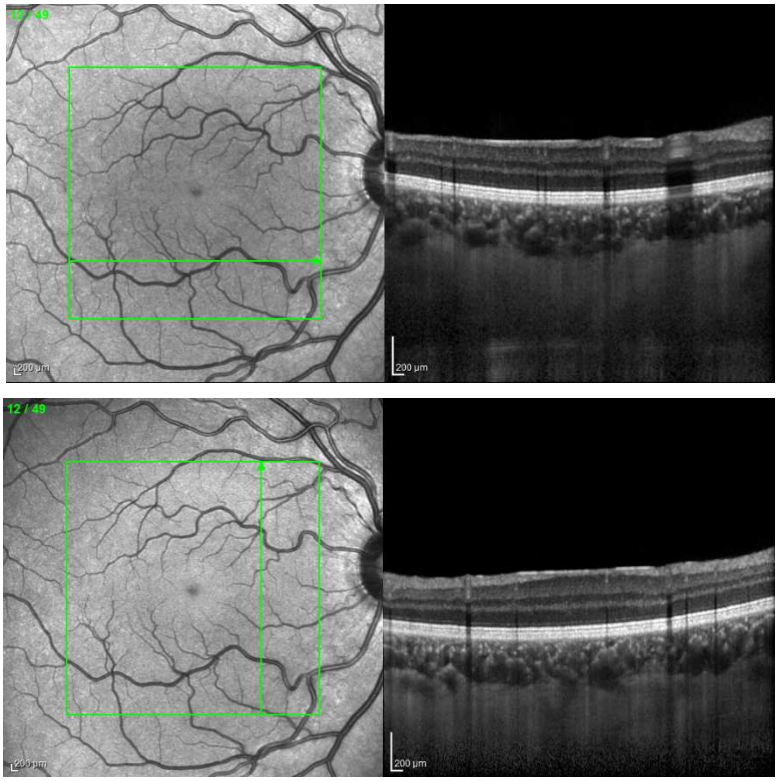

Figure 4.1 – Examples of frames from two orthogonal sets of OCT B-scans acquired from the same eye. On the left, there are the IR images that locate the B-scans (on the right). Plotted in green on the IR image, we can see a square that locates the area scanned by the set of 49 images, as well as an arrow that locates the current B-scan and its scanning direction.

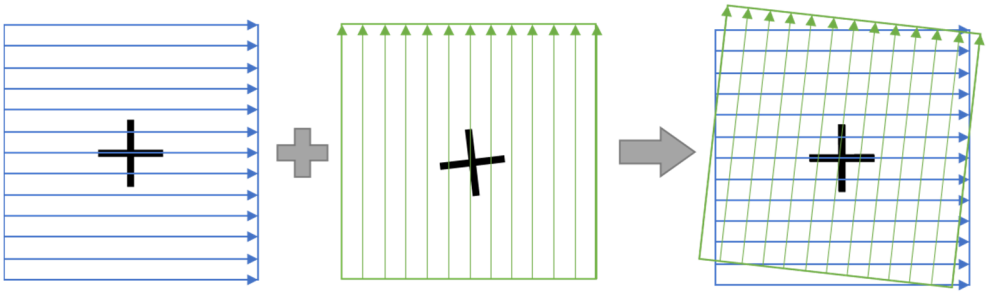

Figure 4.2 - Representation of the locations of two B-cans' sets acquired horizontally and vertically. The final image exemplifies the result of the alignment necessary to merge the information of both sets of scans.

The choroidal thickness information of both directions is integrated by interpolating the values generated in every B-scan, in order to have an equal resolution in both directions (vertical and horizontal). This step is required because the number of B-scans in a set is normally lower than the number of A-scans in a B-scan.

The two sets of B-scans correspond to two separate acquisitions and the automatic alignment between B-scans only occurs within an acquisition, so misalignments between the two sets must be corrected. Because the two sets of B-scans are accompanied with a corresponding IR image of the retinal fundus that locates the scans' position (as seen in Figure 4.1), the alignment can be made using the two IRs. The transformation matrix that spatially aligns the two IR images is found using an iterative intensity based image registration method.

4.2 - Alignment

The alignment of the B-scans is based on the IR images of the retina that locate the tomographic images in the eye surface. The section of the video frames that corresponds to the scanned retinal area is automatically selected (according to the green lines that delimit it, seen in Figure 4.1) for each set of B-scans. These selected IR sections are then used to calculate the transformation matrix that aligns the sets of B-scans.

The transformation matrix is obtained using an image registration algorithm included in the Image Processing Toolbox™ of MATLAB®. This algorithm is an iterative process that tries to maximize the mutual information (as defined by Mattes[32]) calculated from the images' intensities, being suitable for images where the illumination is different. The transformation is deliberately limited to translation and rotation movements, because these are expected to vary in different acquisitions (that are roughly centered in the fovea). The differences in the initial IR images and the result of this alignment can be seen in Figure 4.3 where both IR images are merged to make the differences more visible. Since the scanning areas of the OCT are different, some regions can have information in just one direction. This lack of information can be observed in Figure 4.3 (b) where some triangular regions close to the border are darker (the rotated image has no information in that area).

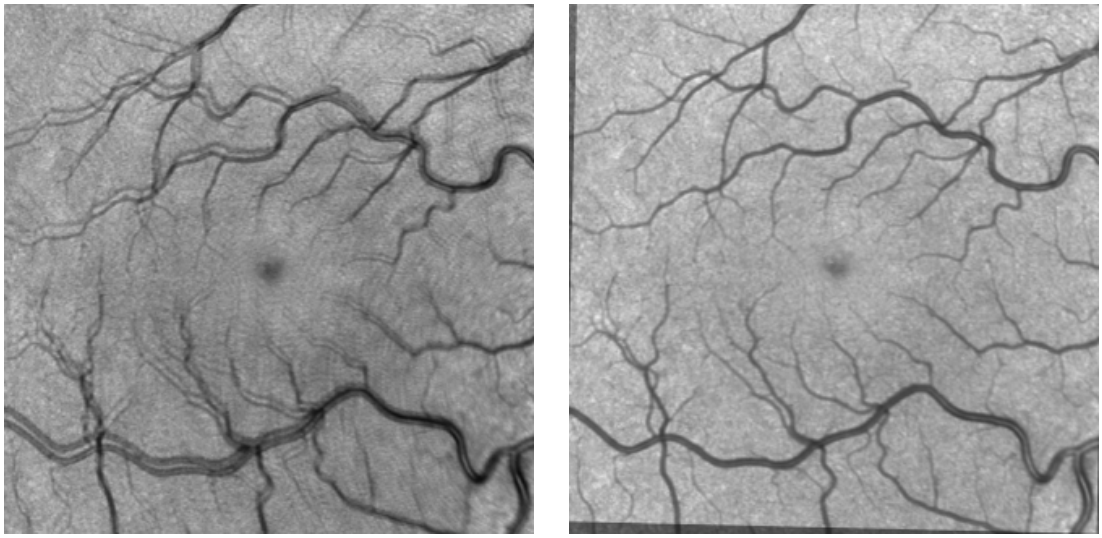

(a) (b)

Figure 4.3 – Example of the overlapping IR images that represent the scanned area by the OCT. (a) original IR images of two OCT videos of the same eye are merged in one representation; (b) the IR images are aligned using the image registration method.

The final choroidal data is also registered using the same transform matrix, after the 3D interpolation. Consequently, the comparison between the segmentations of the choroid in the different directions can be made for the same area of the eye.

4.3 - 3D interpolation

A 3D interpolation method is used to combine the location of the BM and CSI layers of the B-scans in each set, by making an equal number of samples in the B-scan's horizontal axis and its perpendicular axis. A smoothing factor is added to avoid the unnatural transitions between B-scans and filter some abnormal data that could be the cause of future errors.

In order to create a membrane-like surface for the limits of the choroid, a cubic smoothing spline is used as the interpolation method to connect the B-scans in one direction. This method interpolates data and smooths it in order to minimize the squared distance to the samples and a roughness measure (integral of the squared second derivative of the interpolated data) using third-order polynomials. A smoothing parameter p defines the relative weight of the least mean squares (and p´s complement, as the weight for the roughness measure) and it is automatically defined by $p = \left(1 + \frac{h^3}{6}\right)^{-1}$, where h is the spacing between the original data sites, different in the two directions.

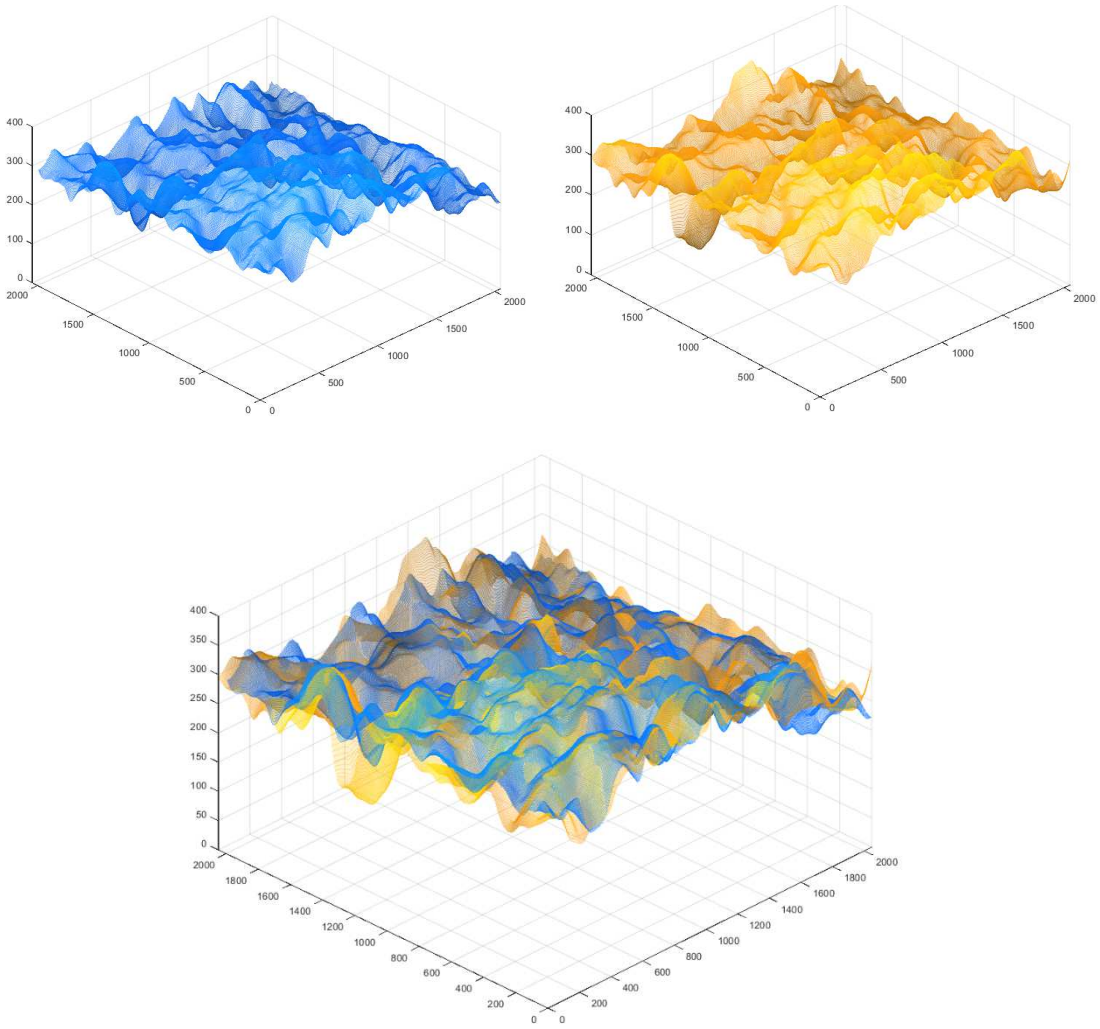

Figure 4.4 – 3D plots of the interpolated choroidal thickness of two perpendicular B-scan series, and the merging of the two, after alignment (axes values are in μm).

After the interpolation, the locations of the limiting boundaries are not only a series of individual lines but a connected surface that can be represented in a 3D plot or a colored image like the one in Figure 4.4. The normalization of the sampling enables a direct comparison between the results in both directions after the alignment transformation is applied.

4.4 - Manual adjustment

When the segmentations in the two directions are compared for the same areas, there are some locations where the final results can have significant inconsistencies (as seen in the example in Figure 4.5). The inconsistencies detected can be solely due to the different directions of the tomographic images. A vessel entering the choroid can be considered as part of the choroid or not depending on the size and shape of the section that is represented in the B-scan.

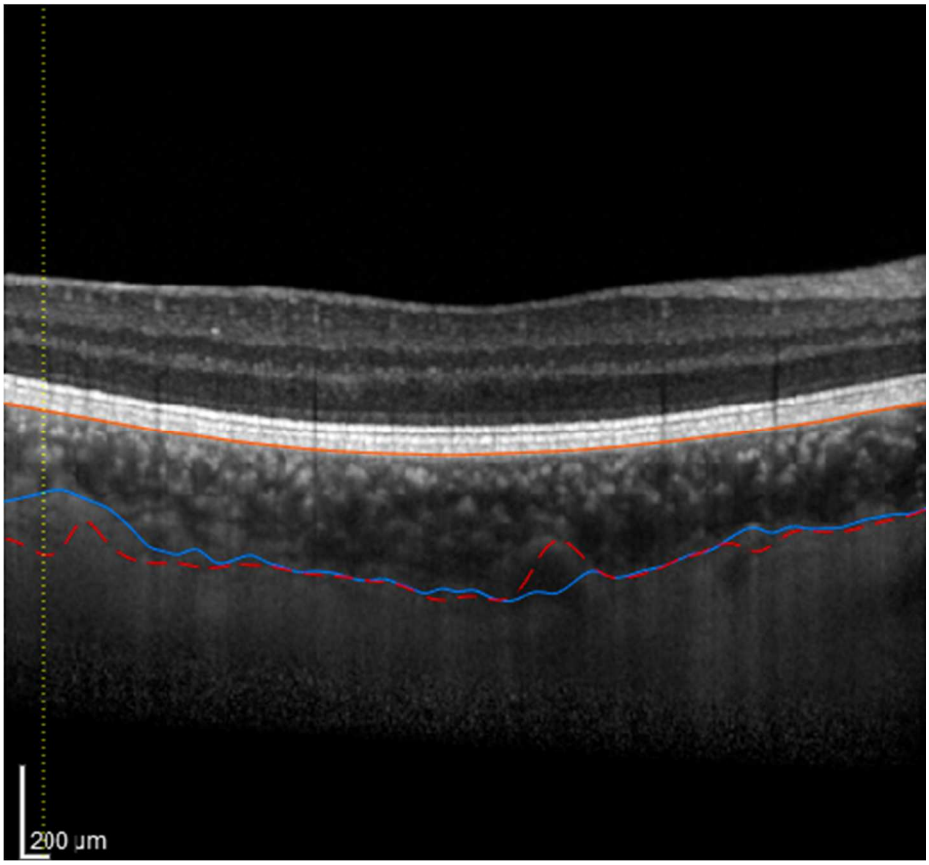

Figure 4.5 – Example of an OCT B-scan with plots of the choroidal boundaries. In orange, the BM; in blue the CSI; the dotted red line represents the interception of the CSI membrane calculated using the series of B-scans in the perpendicular direction; the yellow dotted line is in the column where the difference between the blue and the dotted red lines are maximum.

To avoid major errors in the algorithm, an option to manually correct some areas of the path was added. The experience and expertise of the ophthalmologist may compensate some errors caused by a reduced quality of the image.

Chapter 5

Graphical User Interface

To facilitate the operation of the software system, a Graphical User Interface (GUI) was created. It is divided into two parts: one to input data and the other to show and analyze results.

In the data input part, the user selects the OCT video, the resolutions and the B-scans' direction. The user can input only one video - with one set of B-scans - or two - if the two acquisitions are from the same eye.

After data selection, the processing begins and a new window shows the processing progress. When the processing ends, a new window appears showing the final results. The new window is different depending on the number of input videos, one or two. The final window shows the segmented images and their localization in the IR image. When there are two videos, the location of a selected B-scan's intersection is plotted over the other one.

The choroidal thickness is calculated in the current B-scan and in the whole OCT. To measure just a part of the B-scan, the user has the option to select a section of the paths.

If the user does not agree with the automatic segmentation of the choroid, he can select part of a boundary and retrace it according to his judgment.

5.1 - Data Input

The first window to open has buttons for the options of selecting one or two OCT videos. Then, a new window opens for the file selection. The files to select are limited to 15 of the common video formats, such as AVI, MP4, MPEG, WMV or QuickTime, which the used function can separate in frames). The videos should be extracted from a Heidelberg Spectralis and contain the OCT B-scans, one per frame, scanned in parallel (horizontally or vertically).

If the user wants to select two videos, he can select them separately or at the same time. The two videos must be from the same eye, because the scanning alignment is made with the IR images of both videos and the retina has to be the same.

After the selection of a video, the IR image and the first B scan appear in the interface. The window shown in Figure 5.1 allows the user to verify if the automatic cropping of the IR and B-scans was properly done. Here, the direction of the scans and the three different resolutions should be entered – the longitudinal (or horizontal) and axial (or vertical) resolutions of the OCT and the IR's resolution.

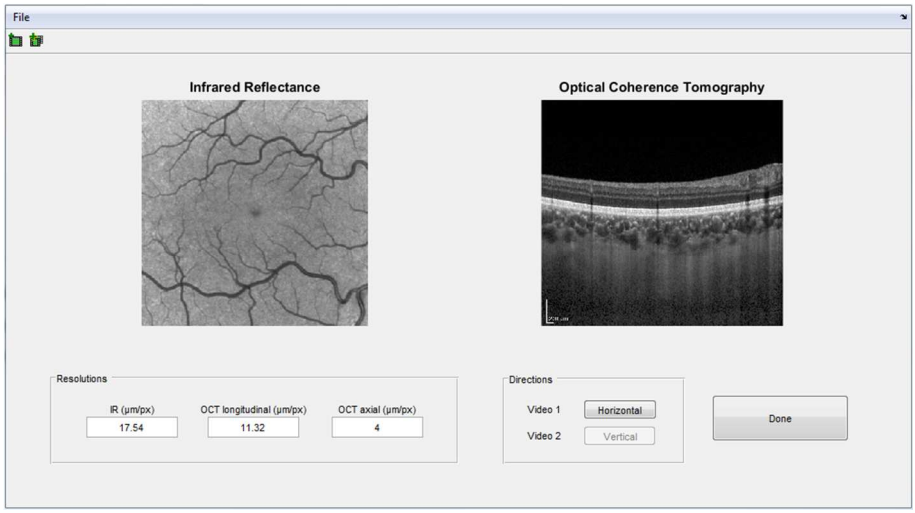

Figure 5.1 – Example of the GUI initial window, after the selection of a video.

As exemplified in Figure 5.2, if the user adds 2 videos, the first B-scan appears in the interface as well as a superimposed image of the aligned IR images. In this case, the user can also verify if the alignment was properly made.

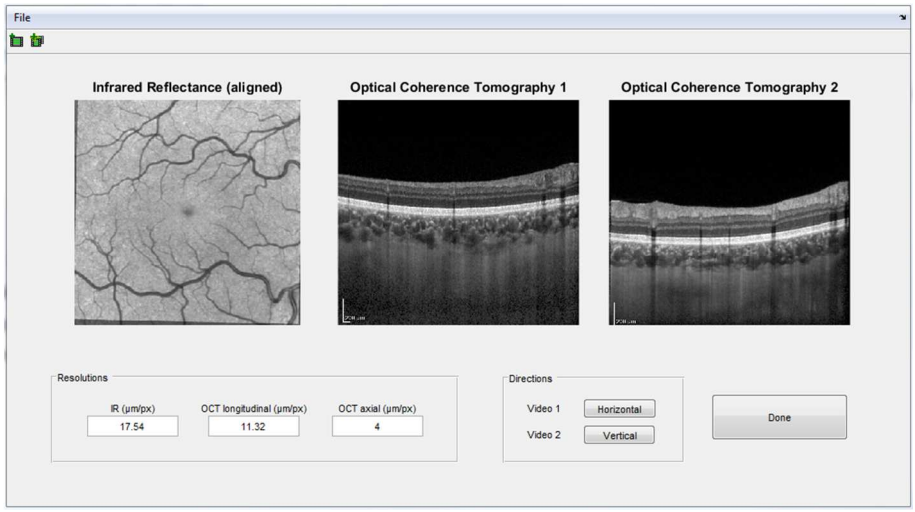

Figure 5.2 - Example of the GUI initial window, after the selection of two videos.

Pressing the button "Done", the user triggers the start of the scans' processing for the choroidal segmentation.

5.2 - Result Analysis

While the processing is occurring, a progress bar, like one in Figure 5.3, informs the user about the relative progression of the processing.

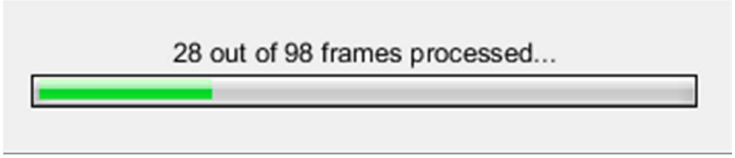

Figure 5.3 – Progress bar showing the processing development.

When the processing ends and the progress bar closes, a new window opens displaying the results. This window is different according to the number of videos selected by the user.

To display the results of one video, the B-scans and the plotted choroidal limits appear in the right, while the IR and the location of the selected B-scan appears on the left, as exemplified in Figure 5.4.

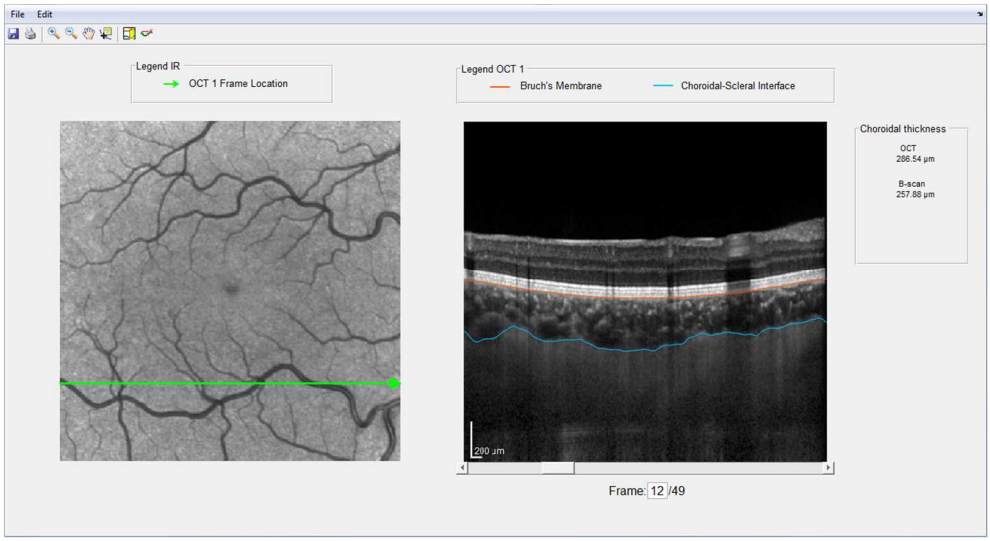

Figure 5.4 – Example of a results window when only one video is selected.

The B-scan selection is either made by editing the number of the frame or moving the slide bar accordingly. The location of the B-scan is detailed by a green arrow in the IR image. The direction of the green arrow represents the progression of the B-scan's columns.

The mean choroidal thickness in the whole OCT and the selected B-scan are presented in the right panel, as soon as the results appear.

If the user wants to measure only a section of the B-scan, he can choose the "Measure section" option, (indicated by the second to last icon, in the icon bar).

As shown in Figure 5.5, two vertical red bars will appear in the OCT, for the selection of the section to measure. These red bars can be dragged by the user to select the desired section. In the right panel, a new entry appears, to display the average thickness of the selected section and it is updated every time the red bars are being dragged.

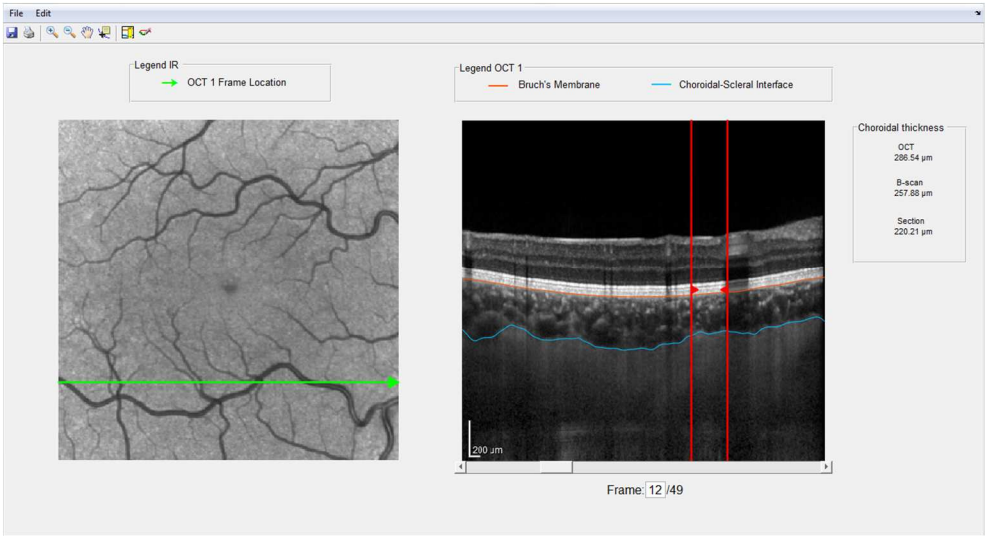

Figure 5.5 – Example of a section measuring window, where the section is selected by dragging the red bars that limit it. The section thickness is shown in the textbox in the right.

There is another option that allows the user to edit a section of the path. When the option "Edit path" is chosen, red vertical lines appear to select the section to edit. To choose between the BM and CSI, the user drags the red line with the mouse pointer closer to the wanted path, and the arrow marker indicates the path to edit. In Figure 5.6, the user is selecting a part of the CSI boundary to edit, as pointed out by the arrow markers.

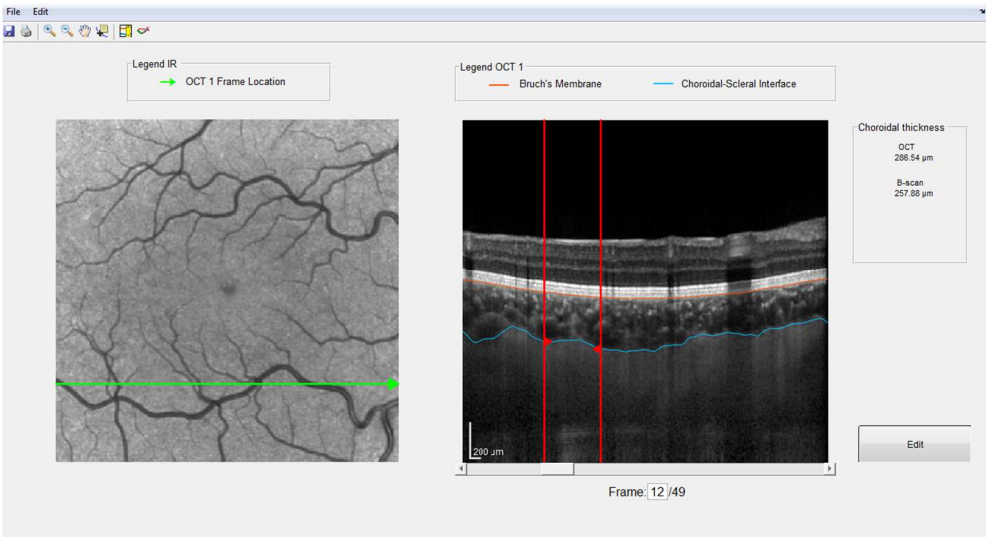

Figure 5.6 – Selection of the path to edit. In this case the editing would occur in the section of the CSI (blue line) between the two red vertical lines.

After manually editing the path, the user must confirm the alterations made. The newly drawn path can be unconnected to the automatic sub-paths that limit it. To guarantee a proper connection in the boundaries, the processing of the B-scan layers has to be ran again.

In case the user selects two videos, the created results window is different, as seen in Figure 5.7. In the left, there is an IR image (from video 1) with the location of the B-scans selected from each of the videos. The arrow in green and yellow locate the B-scan of video 1 and video 2, respectively. The yellow arrow may be displaced because the IR image is obtained from video 1 and the transformation made to align the IR images may displace it.

The two B-scans are shown on the right side and can be selected by writing the frame number or sliding the bar underneath it. In the B-scans there are two additional plotted lines, the red dashed line (that represents the CSI path interpolated by the crossing paths on the other direction) and a dotted vertical yellow or green lines (showing the location that the other selected B-scan crosses).

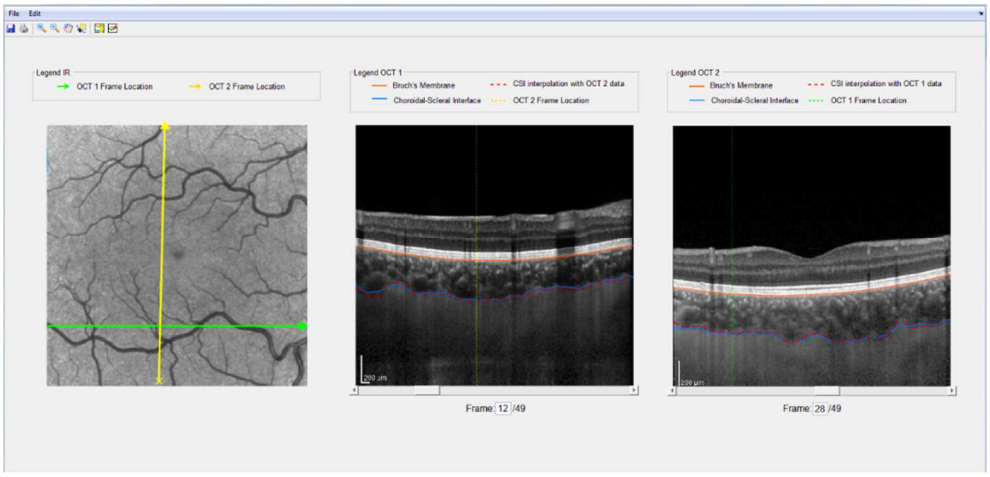

Figure 5.7 – Example of a results window when two videos are selected.

This GUI allows the user to take advantage of the software's features and it generates a tool to add useful information about choroidal OCT images.

Chapter 6

Results and Discussion

To evaluate the performance of the automatic delineation of the CSI, the results of the algorithm were compared with obtained manual markings. The manual boundaries were delineated by ophthalmologists that are accustomed with the OCT technique. Unfortunately, from the two sets of 49 B-scans (horizontal and vertical), only 7 of each have manual segmentations. However, each of them has two manual boundaries as a ground truth, from two different medical doctors, which allowed an analysis of the manual boundary variability and a comparison to the automatic detected CSI.

The differences between two delineations were compared by calculating the mean absolute error $\overline{|\varepsilon|}$ between the paths in each column. The error ratio r is calculated to have a relative measure of agreement between the automatic and manual markings.

As observable in Figure 6.1, there are B-scans where the similarity between the two markings is clearly visible (Figure 6.1 (a)) and others where even the manual markings can have great discrepancies in certain areas (Figure 6.1 (b)). These images can also show the difficulty to have a clear ground truth to evaluate the automatic algorithms.

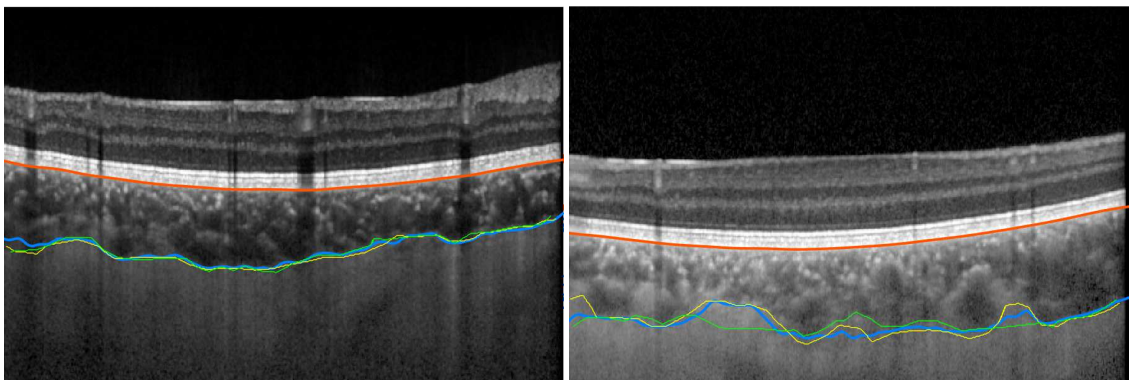

(a) (b)

Figure 6.1 – Two examples of OCT images with plots of the automatically detected choroidal boundaries (orange and blue) and the two manual markings (yellow and green) on the respective OCT B-scans.

The obtained results for the means and the standard deviations of the absolute errors are presented in Table 6.1. The values of $\overline{|\varepsilon_M|}$ are the mean absolute errors measurement between the two manual markings in each frame and $\overline{|\varepsilon_1|}$ is the same error between the automatic and the manual delineations of one doctor and $\overline{|\varepsilon_2|}$ of the other. The measure r –present in the last column is the ratio between the average of the two errors for the automatic markings ($\overline{|\varepsilon_1|}$ and $\overline{|\varepsilon_2|}$) and the one between the two manual ones ($\overline{|\varepsilon_M|}$). The final line shows the averages and standard deviations of the three errors and ratio in all frames.

Table 6.1 – Results of the mean absolute error and the errors ratio of the 14 frames with manual markings as well as the mean (μ) and standard deviation (σ) of each measurement throughout the frames. The values of $\overline{|\varepsilon_M|}$, $\overline{|\varepsilon_1|}$ and $\overline{|\varepsilon_2|}$ are presented in μm; the ratio r is dimensionless.

Frame	$\overline{\lvert\varepsilon_M\rvert}$ (μm)	$\overline{\lvert\varepsilon_1\rvert}$ (μm)	$\overline{\lvert\varepsilon_2\rvert}$ (μm)	$r = \frac{\overline{\lvert\varepsilon_1\rvert} + \overline{\lvert\varepsilon_2\rvert}}{2 \cdot \overline{\lvert\varepsilon_M\rvert}}$
Horizontal 7	13.7 ±13.3	13.8 ±12.0	15.3 ±15.1	1.07
Horizontal 8	7.06 ±4.86	9.22 ±10.6	10.5 ±10.9	1.40
Horizontal 9	19.9 ±22.5	13.8 ±21.0	16.4 ±14.4	0.759
Horizontal 10	15.8 ±18.5	13.5 ±20.0	9.20 ±7.30	0.717
Horizontal 11	7.40 ±6.15	8.80 ±8.41	8.82 ±7.57	1.19
Horizontal 12	9.99 ±8.78	7.63 ±6.08	7.43 ±6.21	0.754
Horizontal 13	12.0 ±11.2	10.3 ±9.44	8.58 ±8.01	0.785
Vertical 35	9.44 ±7.47	10.5 ±11.0	11.2 ±11.3	1.15
Vertical 36	10.0 ±7.73	12.1 ±11.3	10.3 ±10.9	1.12
Vertical 37	12.9 ±16.0	14.7 ±14.1	12.6 ±11.9	1.06
Vertical 38	20.3 ±21.3	14.6 ±11.8	17.0 ±17.5	0.779
Vertical 39	34.0 ±28.4	16.0 ±14.6	25.8 ±25.7	0.616
Vertical 40	15.3 ±13.1	15.4 ±11.7	11.2 ±8.70	0.865
Vertical 41	14.2 ±10.6	12.2 ±9.68	11.7 ±11.0	0.846
$\mu \pm \sigma$	14.4 ± 16.5	12.3 ±12.6	12.6 ±13.7	0.937 ±0.227

The results show that the errors for the automatic segmentation are always comparable to the ones between the manual ones. The averages of the errors in all frames, presented in the last column, show that even both $\overline{|\varepsilon_1|}$ and $\overline{|\varepsilon_2|}$ averages are smaller than the average $\overline{|\varepsilon_M|}$. Both the median (0.856) and the average of the error ratios are smaller than one, leading to the conclusion that this algorithm agrees with the manual markings.

Since the manual markings were only present in a small group of B-scans of the two sets, a different kind of measurement was thought to evaluate the algorithm. The availability of two parallel sets of B-scans in the same eye allowed a comparison of the choroidal segmentations from different acquisitions.

After the 3D interpolation and registration of the choroidal boundaries, the differences between the CSI boundaries of each set were calculated, using the BM as a reference An image representation of this difference is presented in Figure 6.2, where the values of the 3D surface corresponds to the color variation.

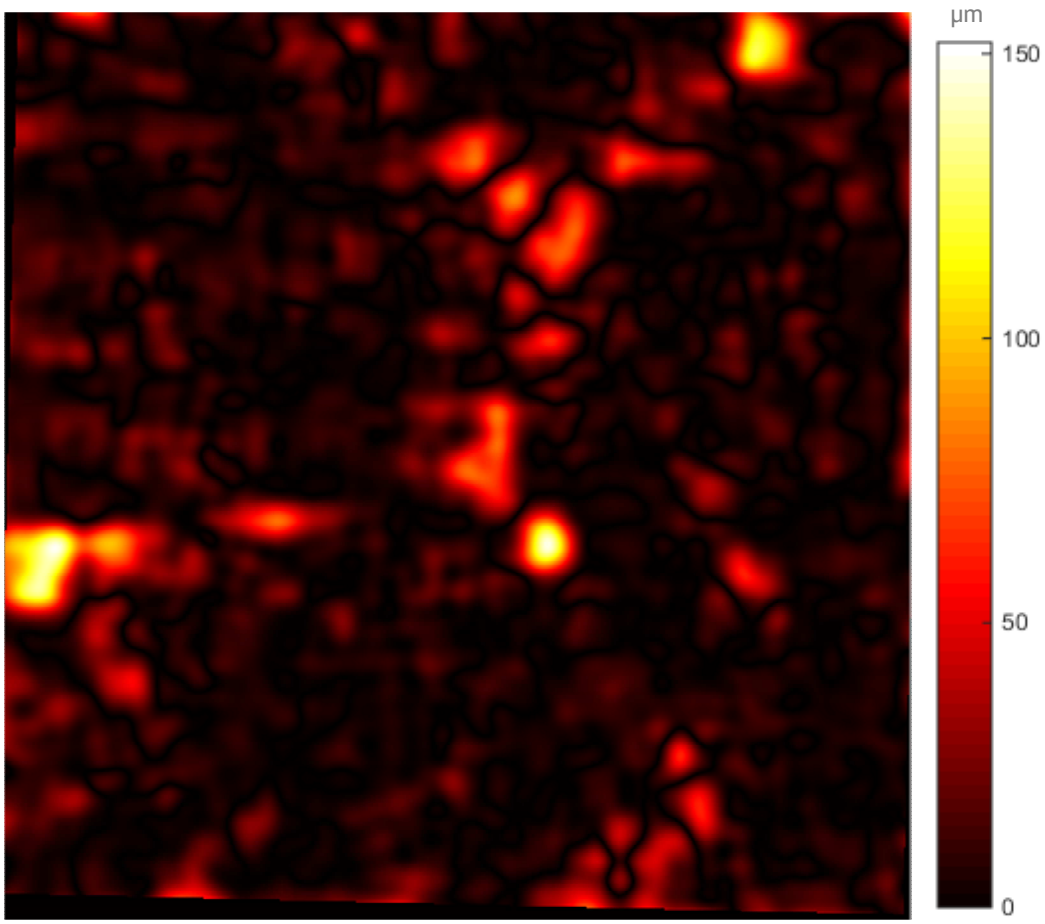

Figure 6.2 – Image representing the absolute differences between the two 3D interpolated boundaries. The axes of this image are correspondent to those in the IR image. The colors range from dark red to light yellow corresponding to values from 0 µm to 152 µm as expressed in the color bar on the right.

A histogram of the errors is presented in Figure 6.3. The histogram allows an easier analysis of the errors distribution in the previous image although ignoring the location information.

The mean absolute error between the two surfaces that represent the choroidal thickness is approximately 11.49 µm while the median is 6.45 µm, meaning that the majority of values have less than 2.2% of the average choroidal thickness in the analyzed eye (288.54 µm).

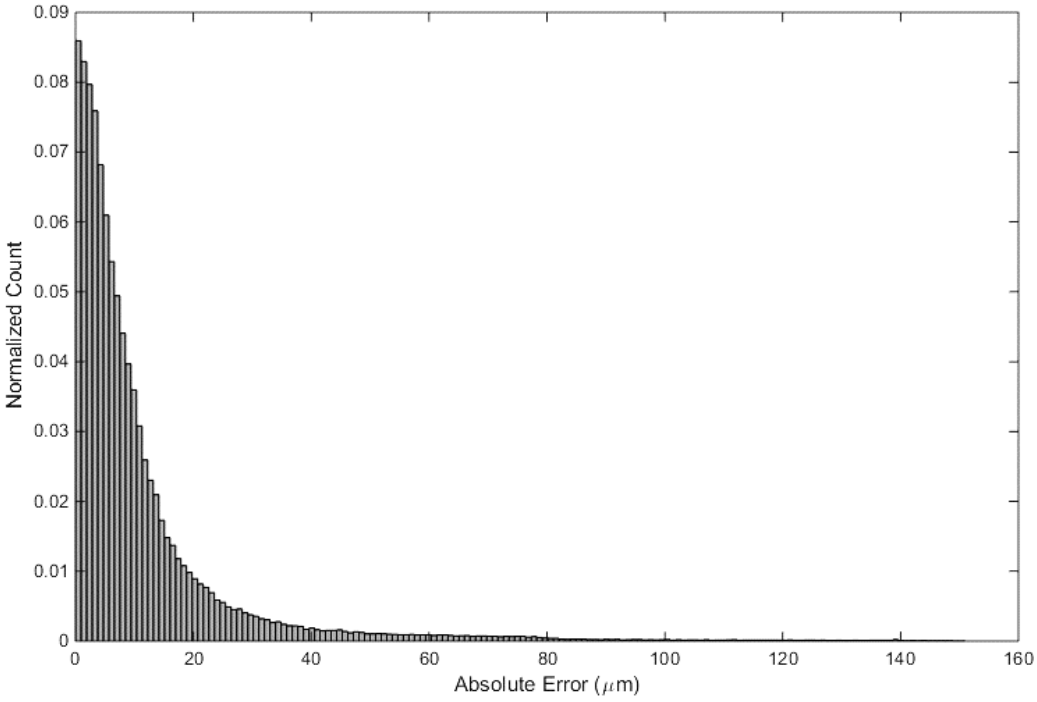

Figure 6.3 – Histogram of the values of the differences between the two aligned CSI surfaces. The normalized count is the number of pixels with that error value divided by the total number of valid pixels.

The possibility of manually correcting the automatic delineations allows the decrease of the larger differences between the two directions and brings the mean to lower values and, as seen in Figure 6.2, the highest error values are located in very specific regions.

The errors between the two directions can be caused by the way a vessel is sectioned in the tomographic image, in one direction it may seem as part of the choroid while in the other it may seem as a separate incoming vessel. This kind of errors can also cause an incorrect manual delineation, because in the normal OCT analysis, the ophthalmologist does not make this kind of comparison between different sets of B-scans, only comparing a B-scan with the adjacent ones of the same set.

Figure 6.4 and Figure 6.5 are examples of good and not so good similarity between the path calculated in the presented B-scan and the interpolated path created with the values from the perpendicular B-scans that cross this frame.

In the OCT B-scans presented in Figure 6.4, there are not very dubious areas for the tracing of the CSI. In this B-scans, both directions marked the CSI relatively in a similar spot according to the BM layer. The shadows in these frames are not too significant and vessels in the sclera are far enough to be excluded from being classified as part of the choroid.

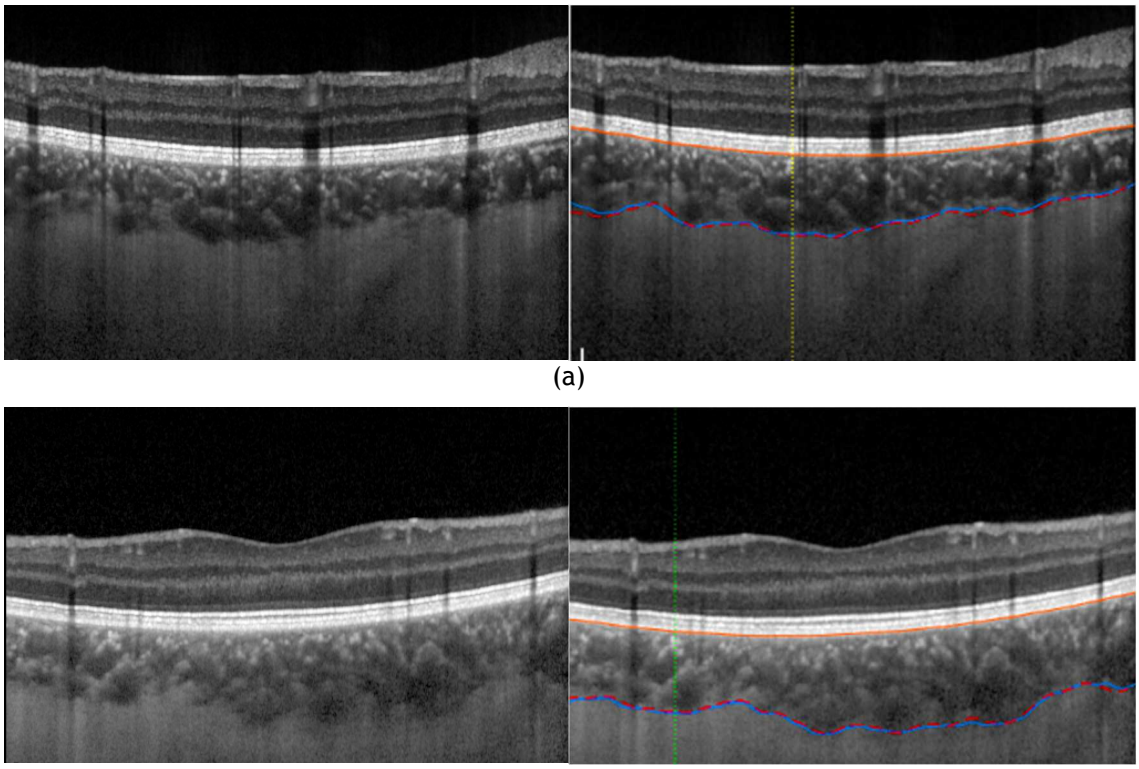

(a)

(b)

Figure 6.4 – Examples of two perpendicular B-scans; in the right image, plotted in orange is represented the BM and in blue, the CSI calculated in the respective B-scan. The red dashed line represents the path interpolated with the matching sites of the perpendicular set of B-scans. The vertical dotted yellow and green lines are the locations where the other B-scan crosses as explained in Chapter 5.

Figure 6.5 shows two B-scans with some areas where the algorithm did not completely agree in the location of the CSI. The two B-scans cross in the point of higher difference in choroidal thickness between the two directions of OCT frames. This higher error seems to be caused by the surrounding areas. In Figure 6.5 (a), the blue path seems to be the obvious path, however, in the corresponding place in Figure 6.5 (b) the blue line looks like the most correct as well (as the red dashed line has a big inflection and excludes some dubious areas).

In fact, the two images were analyzed by an ophthalmologist and the clinician did not disagree with either automatic delineations. The fact that the correct delineation continued to be dubious was the main reason for the inclusion of a manual correction after the presentation of the final results. In this way, medical doctors can decide on the most adequate path to segment the choroid, according to their personal perspective and experience.

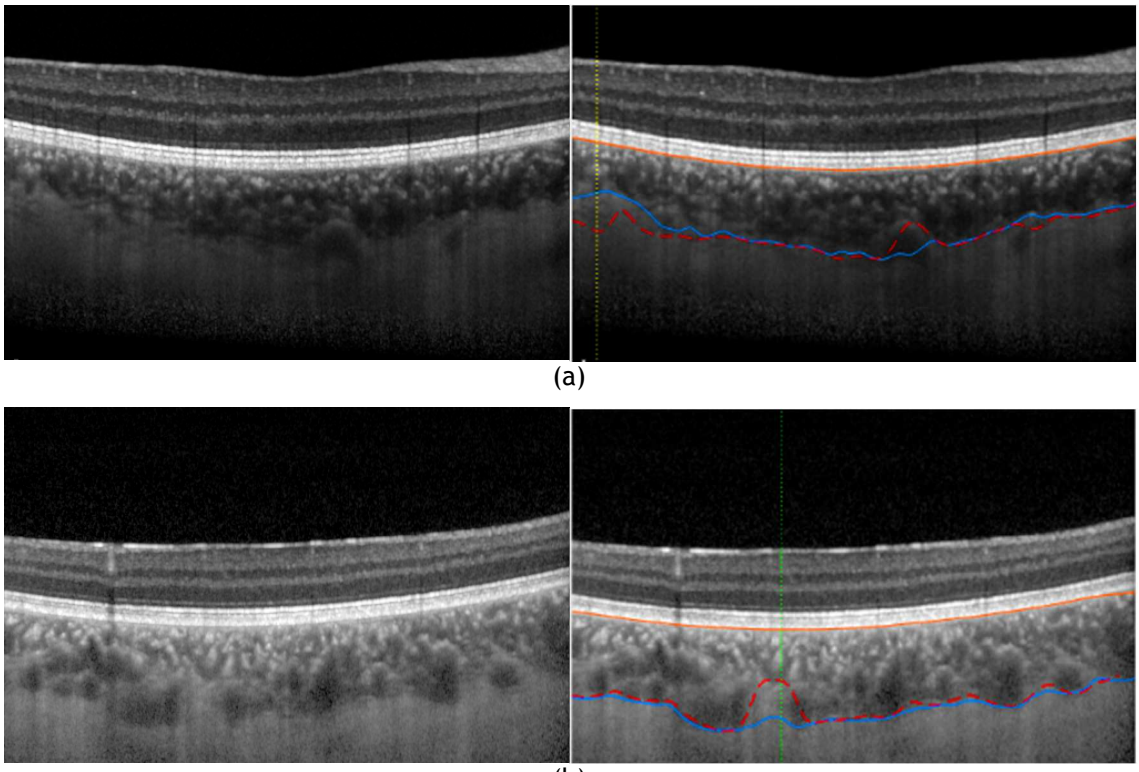

Figure 6.5 – Examples of two perpendicular B-scans; on the right, plotted in orange is represented the BM and in blue, the CSI calculated in the respective B-scan. The red dashed line is the path interpolated with the detected values of the perpendicular set of B-scans that cross the B-scan. The vertical dotted yellow and green lines are the locations where the other B-scan crosses as explained in Chapter 5.

The final results were very satisfying, both visually and by comparing with the manual markings and with the perpendicular B-scans. However, this algorithm was only tested for one relatively healthy eye. Testing OCT images of eyes with different kinds of disease may cause the appearance of some errors because some diseases that affect the eye globe can distort its layers (like retinal detachment or big drusen).

Chapter 7

Conclusion

The proposed objectives for this thesis were successfully achieved. The choroidal thickness was accurately calculated by the automatic detection of the internal and external boundaries (the BM and CSI) with the developed software system.

The boundaries are calculated using an algorithm, based on a dynamic programming method, for the calculation of the lowest cost path between the lateral limits of the B-scans. The costs of the paths between nodes are defined by a weight matrix, resulting from the manipulation of the original B-scan (according to the boundary's properties). The weights in the matrix are proportionately inverse to the likelihood of belonging to the boundary, with the objective of achieving a continuous path that is the closest to the true boundary.

The preprocessing part of the software includes denoising, contrast adjustment, image flattening and region of interest selection. The denoising was based on the stationary wavelet transform and allowed a directional denoising, avoiding the softening of the vertical transitions, but decreasing the noise and the transitions induced by the projected shadows. The contrast adjustment not only helped to enhance each transition but also managed to reduce the shadows cast by retinal vessels. The flattening and region selection was done after the location of the BM and was useful to reduce the area to find the CSI and normalize the B-scan according to the BM's position.

The calculation of the choroidal thickness is the average of the vertical distance between its limits. However, in the developed software there is an option to measure the choroidal thickness in a selected area.

The dataset of OCT images allowed an interpolation of the delineated boundaries to make a 3D surface. Since the dataset included two sets of the same eye, it was possible to align the B-scans and compare the segmentations in two perpendicular directions.

There was a good correspondence between the two calculated choroidal thicknesses (from perpendicular sets of B-scans). However, some areas of the choroid, harder to manually segment, had higher differences, although those regions were rare in the final results.

The final results of the automatic choroidal segmentation were very adequate. When the automatic results were compared with the available manual segmentations were equivalent to the variances between the two manual boundaries.

In future development of this work, the robustness of this algorithm should be tested. Although the number of tested B-scans was relatively large (98), the software was developed with only one set of B-scans of the same healthy eye and using the same method of acquisition. It is possible that there could be a different success rate when different EDI-OCT scans are set as input. The software is prepared to receive other types of settings in the input image, but these alterations were not tested during the development of the present work.

A bigger set of images with ground truth to both boundaries would also be beneficial to the testing of the final results (even for the confirmation of the BM layer), allowing a comparison to other algorithms found in the literature. The best case scenario would be to have access to a public dataset, of which other authors could compare results.

Generally, the goals for this project were achieved, despite the fact that future work should be done in order to improve some details and test larger and more diverse datasets.

References

[1] Y. Imamura, T. Fujiwara, R. Margolis, and R. F. Spaide, “Enhanced depth imaging optical coherence tomography of the choroid in central serous chorioretinopathy.,” Retina, vol. 29, no. 10, pp. 1469–73, Jan. .

[2] D. S. Dhoot, S. Huo, A. Yuan, D. Xu, S. Srivistava, J. P. Ehlers, E. Traboulsi, and P. K. Kaiser, “Evaluation of choroidal thickness in retinitis pigmentosa using enhanced depth imaging optical coherence tomography.,” Br. J. Ophthalmol., vol. 97, no. 1, pp. 66–9, Jan. 2013.

[3] M. Esmaeelpour, B. Považay, B. Hermann, B. Hofer, V. Kajic, S. L. Hale, R. V North, W. Drexler, and N. J. L. Sheen, “Mapping choroidal and retinal thickness variation in type 2 diabetes using three-dimensional 1060-nm optical coherence tomography.,” Invest. Ophthalmol. Vis. Sci., vol. 52, no. 8, pp. 5311–6, Jul. 2011.

[4] Y. Ikuno and Y. Tano, “Retinal and choroidal biometry in highly myopic eyes with spectral-domain optical coherence tomography.,” Invest. Ophthalmol. Vis. Sci., vol. 50, no. 8, pp. 3876–80, Aug. 2009.

[5] V. Manjunath, M. Taha, J. G. Fujimoto, and J. S. Duker, “Choroidal thickness in normal eyes measured using Cirrus HD optical coherence tomography.,” Am. J. Ophthalmol., vol. 150, no. 3, pp. 325–329.e1, Sep. 2010.

[6] D. L. Nickla and J. Wallman, “The multifunctional choroid.,” Prog. Retin. Eye Res., vol. 29, no. 2, pp. 144–68, Mar. 2010.

[7] G. Staurenghi, S. Sadda, U. Chakravarthy, and R. F. Spaide, “Proposed Lexicon for Anatomic Landmarks in Normal Posterior Segment Spectral-Domain Optical Coherence Tomography: The IN•OCT Consensus,” Ophthalmology, vol. 121, no. 8, pp. 1572–1578, 2014.

[8] “Thorlabs - Optical Coherence Tomography Tutorial.” [Online]. Available: http://www.thorlabs.com/images/TabImages/1742_figure1_780.jpg. [Accessed: 01-Jun-2016].

[9] D. Huang, E. A. Swanson, C. P. Lin, J. S. Schuman, W. G. Stinson, W. Chang, M. R. Hee, T. Flotte, K. Gregory, and C. A. Puliafito, “Optical coherence tomography.,” Science, vol. 254, no. 5035, pp. 1178–81, Nov. 1991.

[10] S. Yun, G. Tearney, J. de Boer, N. Iftimia, and B. Bouma, “High-speed optical frequency-domain imaging,” Opt. Express, vol. 11, no. 22, p. 2953, Nov. 2003.

[11] H. G. Bezerra, M. A. Costa, G. Guagliumi, A. M. Rollins, and D. I. Simon, “Intracoronary Optical Coherence Tomography: A Comprehensive Review. Clinical and Research Applications,” JACC: Cardiovascular Interventions, vol. 2, no. 11. pp. 1035–1046, Nov-2009.

[12] T. Torzicky, M. Pircher, S. Zotter, M. Bonesi, E. Götzinger, and C. K. Hitzenberger, “Automated measurement of choroidal thickness in the human eye by polarization sensitive optical coherence tomography.,” Opt. Express, vol. 20, no. 7, pp. 7564–74, Mar. 2012.

[13] R. F. Spaide, H. Koizumi, and M. C. Pozonni, “Enhanced Depth Imaging Spectral-Domain Optical Coherence Tomography,” Am. J. Ophthalmol., vol. 146, no. 4, pp. 496–500, 2008.

[14] H. Lu, N. Boonarpha, M. T. Kwong, and Y. Zheng, “Automated segmentation of the choroid in retinal optical coherence tomography images.,” Conf. Proc. Annu. Int. Conf. IEEE Eng. Med. Biol. Soc. IEEE Eng. Med. Biol. Soc. Annu. Conf., vol. 2013, pp. 5869–72, Jan. 2013.

[15] Z. Hu, X. Wu, Y. Y. Ouyang, Y. Y. Ouyang, and S. R. Sadda, “Semiautomated segmentation of the choroid in spectral-domain optical coherence tomography volume scans.,” Invest. Ophthalmol. Vis. Sci., vol. 54, no. 3, pp. 1722–9, Mar. 2013.

[16] S. J. Chiu, X. T. Li, P. Nicholas, C. A. Toth, J. A. Izatt, and S. Farsiu, “Automatic segmentation of seven retinal layers in SDOCT images congruent with expert manual segmentation.,” Opt. Express, vol. 18, no. 18, pp. 19413–28, Aug. 2010.

[17] P. Massin, A. Erginay, B. Haouchine, A. Ben Mehidi, M. Paques, and A. Gaudric, “Retinal thickness in healthy and diabetic subjects measured using optical coherence tomography mapping software.,” Eur. J. Ophthalmol., vol. 12, no. 2, pp. 102–8, Jan. 2002.

[18] D. Cabrera Fernández, H. M. Salinas, and C. A. Puliafito, “Automated detection of retinal layer structures on optical coherence tomography images,” Opt. Express, vol. 13, no. 25, p. 10200, Dec. 2005.

[19] L. Duan, M. Yamanari, and Y. Yasuno, “Automated phase retardation oriented segmentation of chorio-scleral interface by polarization sensitive optical coherence tomography,” Opt. Express, vol. 20, no. 3, p. 3353, Jan. 2012.

[20] D. Alonso-Caneiro, S. A. Read, and M. J. Collins, “Automatic segmentation of choroidal thickness in optical coherence tomography.,” Biomed. Opt. Express, vol. 4, no. 12, pp. 2795–812, Dec. 2013.

[21] J. Tian, P. Marziliano, M. Baskaran, T. A. Tun, and T. Aung, “Automatic segmentation of the choroid in enhanced depth imaging optical coherence tomography images.,” Biomed. Opt. Express, vol. 4, no. 3, pp. 397–411, Mar. 2013.

[22] M. J. A. Girard, N. G. Strouthidis, C. R. Ethier, and J. M. Mari, “Shadow removal and contrast enhancement in optical coherence tomography images of the human optic nerve head.,” Invest. Ophthalmol. Vis. Sci., vol. 52, no. 10, pp. 7738–48, Sep. 2011.

[23] P. Arbeláez, M. Maire, C. Fowlkes, and J. Malik, “Contour detection and hierarchical image segmentation.,” IEEE Trans. Pattern Anal. Mach. Intell., vol. 33, no. 5, pp. 898–916, May 2011.

[24] V. Kajić, M. Esmaeelpour, B. Považay, D. Marshall, P. L. Rosin, and W. Drexler, “Automated choroidal segmentation of 1060 nm OCT in healthy and pathologic eyes using a statistical model.,” Biomed. Opt. Express, vol. 3, no. 1, pp. 86–103, Jan. 2012.

[25] H. Danesh, R. Kafieh, H. Rabbani, and F. Hajizadeh, “Segmentation of choroidal boundary in enhanced depth imaging OCTs using a multiresolution texture based modeling in graph cuts.,” Comput. Math. Methods Med., vol. 2014, p. 479268, Jan. 2014.

[26] A. González-López, B. Remeseiro, M. Ortega, and M. G. Penedo, “Choroid characterization in EDI OCT retinal images based on texture analysis,” ICAART 2015 - 7th Int. Conf. Agents Artif. Intell. Proc., vol. 2, no. JANUARY, pp. 269–276, 2015.

[27] A. González-López, M. Ortega, M. G. Penedo, and P. Charlón, Image Analysis and Recognition, vol. 8815. Cham: Springer International Publishing, 2014.

[28] L. Zhang, K. Lee, M. Niemeijer, R. F. Mullins, M. Sonka, and M. D. Abràmoff, “Automated segmentation of the choroid from clinical SD-OCT.,” Invest. Ophthalmol. Vis. Sci., vol. 53, no. 12, pp. 7510–9, Nov. 2012.

[29] M. K. Garvin, M. D. Abramoff, R. Kardon, S. R. Russell, X. Wu, and M. Sonka, “Intraretinal layer segmentation of macular optical coherence tomography images using optimal 3-D graph search.,” IEEE Trans. Med. Imaging, vol. 27, no. 10, pp. 1495–505, Oct. 2008.

[30] M. Niemeijer, M. K. Garvin, B. van Ginneken, M. Sonka, and M. D. Abràmoff, “Vessel segmentation in 3D spectral OCT scans of the retina,” in Medical Imaging, 2008, p. 69141R–69141R–8.

[31] L. Zhang, G. H. S. Buitendijk, K. Lee, M. Sonka, H. Springelkamp, A. Hofman, J. R. Vingerling, R. F. Mullins, C. C. W. Klaver, and M. D. Abràmoff, “Validity of Automated Choroidal Segmentation in SS-OCT and SD-OCT.,” Invest. Ophthalmol. Vis. Sci., vol. 56, no. 5, pp. 3202–11, May 2015.

[32] D. Mattes, D. R. Haynor, H. Vesselle, T. K. Lewellyn, and W. Eubank, “Nonrigid multimodality image registration,” Med. Imaging 2001 Image Process., vol. 4322, no. 20 1, pp. 1609–1620, Jul. 2001.